Determining the distance to galaxies using planetary nebulae

José Antonio Ortiz Contreras

Supervisor: Sébastien Comerón Limbourg
Co-Supervisor: Ignacio Trujillo Cabrera

A thesis submitted in partial fulfillment
of the requirements for the degree of
Master in Astrophysics

Departmento de Astrofísica
Universidad De La Laguna
Spain
4 July 2023

Contents

A mis padres,
quienes lo han dado todo por mí.

A mis tres mejores amigos, Rodolfo, Nicolás, y Miguel,
por su comprensión y apoyo.

A Nuna,
quien enseña a mirar la vida con ojos de niño.

Y a mi supervisor y mejor profesor, Sébastien,
por su respaldo y colaboración.

Resumen

Las observaciones son la forma principal de recolectar datos en astronomía, pero no toda la información es directamente accesible. La medición de algunas propiedades de las galaxias o estrellas, como la luminosidad intrínseca o el tamaño físico, depende de sus distancias. Por lo tanto, es fundamental para nuestra comprensión del Universo conocer tales distancias, pero su medición es una tarea delicada. Las distancias cósmicas abarcan muchas órdenes de magnitud, lo que impide el uso de una única técnica para su medición y en su lugar requiere una combinación de técnicas, conocida como la "escala de distancias cósmicas". Desafortunadamente, las incertidumbres en los diferentes peldaños de tal escalera pueden propagarse a técnicas que cubran los objetos más distantes (Freedman, 2021). Por lo tanto, es deseable encontrar técnicas que sean precisas y fácilmente aplicables a un gran número de objetos.

Para galaxias cercanas, el extremo de la rama gigante roja (TRGB), las Cefeidas, las supernovas de Tipo Ia (SNe Ia) y las fluctuaciones en la luminosidad superficial (SBF) son algunas de las técnicas principales utilizadas para obtener distancias precisas, pero métodos redundantes son esenciales para verificar posibles diferencias sistemáticas. Otro método que puede lograr una precisión similar es la función de luminosidad de las nebulosas planetarias (PNLF).

Las nebulosas planetarias se caracterizan por estar ionizadas por estrellas con masas entre 1 y 8 $M_\odot$, durante su evolución desde la rama gigante asintótica hasta la fase de enana blanca. Estas PNe albergan estrellas centrales que emiten con una luminosidad que puede superar los 6000 $L_\odot$, con aproximadamente el 12% de su luminosidad total emitida en la línea [O III] λ5007 Å. La [O III] λ5007 Å PNLF es una relación empírica que predice el número de PNe observadas basándose en su luminosidad. El punto cero M^*, que se determina a partir de la luminosidad de las PNe más brillantes, desempeña un papel crucial en la determinación de distancias con la técnica de la PNLF, mucho más que la forma funcional de la PNLF. Para determinar este valor, se utilizan PNe en galaxias con distancias conocidas, de ahí que la PNLF sea considerada como una candela estándard *secundaria*.

Los instrumentos avanzados de espectroscopía de unidad de campo integral (IFU), como el Multi-Unit Spectroscopic Explorer (MUSE) en el Very Large Telescope (VLT), han revolucionado las mediciones de distancias basadas en PNLF al proporcionar una información espectral completa. MUSE ofrece una mayor sensibilidad, un ancho de banda más estrecho y la capacidad de discriminar entre varios tipos de objetos, facilitando que la técnica basada en la PNLF esté teniendo un renacimiento ya que la información espacial y espectral contenida en los cubos de datos ofrece muchas ventajas sobre la técnica clásica conocida como "narrow-band imaging".

El objetivo del presente trabajo es la determinación de la distancia a la galaxia espiral NGC 628 mediante la estimación de la PNLF con datos de MUSE.

Un reciente estudio por Roth et al. (2021) con datos de MUSE ha demostrado que el uso de la espectroscopía de campo integral permite obtener una precisión sin precedentes en la medición de distancias utilizando nebulosas planetarias. Además, su metodología permite alcanzar distancias de hasta 40 Mpc, el doble de lo que se había podido lograr con anterioridad. En este estudio se ha implementado tal metodología, en particular la técnica denominada Differential Emision Line Filtering (DELF) para la detección de objetos emisores en la línea prohibida de oxígeno [O III] λ5007 Å.

La detección de PNe es difícil debido a la emisión del continuo de la galaxia en imágenes de banda ancha. La metodología DELF, para superar esta dificultad, se basa en una adaptación del

enfoque tradicional con filtros de banda estrecha introducido por Jacoby (1989), y conocida como *on*-band/*off*-band, la cual permite eliminar el brillo del continuo. Roth et al. (2021) refinó este método creando una acumulación (stack) de capas de datos centradas en la línea [O III] λ5007 Å, desplazada por el efecto Doppler según el corrimiento al rojo de la galaxia huésped, de tal forma que el ancho de banda efectivo se ve reducido, mejorando la relación señal-ruido en las detecciones de PNe. Además, el uso de IFU mejora la precisión de la fotometría de las PNe.

La verificación de los objetos candidatos a PNe es crucial para evitar la contaminación de otros objetos, como regiones H II compactas, galaxias de fondo o remanentes de supernovas (SNR). No poder distinguir con precisión estos objetos puede distorsionar el límite brillante M^* de la PNLF y subestimar la distancia a la galaxia. Para distinguir estos contaminantes de nuestra muestra inicial de 1009 objetos candidatos a PNe identificados en los mapas de [O III], se han medido también los flujos en las líneas de Hβ λ4861.33, Hα λ6562.82, [N II] λ6583.46, and [S II] $\lambda\lambda$6716.44, 6730.81. NGC 628 muestra formación estelar en curso, lo que indica que la emisión de [O III] no se debe únicamente a PNe, sino también a regiones H II compactas y SNR. Por tanto, empleando diagnósticos basados en estas líneas de emisión este estudio ha logrado diferenciar y excluir estas fuentes del catálogo de candidatos a PNe: cada clase de objeto (PNe, regiones H II y SNR) tiene una fuente única de radiación ionizante, lo que se refleja en sus espectros con características distintivas. En este estudio se han implementado varios esquemas de clasificación complementarios para distinguir PNe de regiones H II y SNR.

En este estudio se han obtenido tres muestras de PNe en base a estos criterios de clasificación, resultando en $\sim$200 PNe con magnitudes inferiores a 28.0 mag, el límite impuesto a fin de usar la parte más brillante de la PNLF, respectivamente. Tomando como medida representativa de nuestras estimaciones 29.88 ± 0.06, nuestros resultados concuerdan excelentemente con otras distancias basadas en la PNLF.

Nuestros hallazgos apoyan la fiabilidad de la PNLF como una valiosa *standard candle*. Las distancias obtenidas para NGC 628 en este estudio muestran una excelente concordancia con mediciones anteriores, en particular aquellas basadas en la técnica de la PNLF.

Además, en la era de la cosmología de precisión, el uso de la PNLF podría ayudar a abordar la tensión actual entre las medidas locales de la constante de Hubble, a través de la velocidad de recesión de las galaxias cercanas, y los valores derivados del fondo de microondas. En este contexto, la PNLF puede proporcionar una útil verificación cruzada en las mediciones de distancias hasta los $\sim$40 Mpc.

Chapter 1

Introduction

Some fundamental properties of galaxies and stars, such as their intrinsic luminosity or physical size, rely on their distances, which, in turn, also rely on observations for their determination. Therefore, achieving a comprehensive understanding of the universe necessitates precise knowledge of these distances, which can be a challenging endeavour. Given the immense range of cosmic distances, spanning multiple orders of magnitude, a sole measurement of distance is insufficient. Instead, a variety of techniques are used which are referred to as the *cosmic distance ladder*. Unfortunately, the cosmic distance ladder presents its own set of challenges. Flaws or uncertainties in the various steps of the ladder can propagate into significant uncertainties when measuring distances to the most remote objects. This emphasizes the critical need for accurate and broadly applicable techniques that can be employed for a vast number of objects.

When studying galaxy evolution, nearby galaxies within a distance of less than 20 Mpc can be investigated with high physical resolution ranging from 10-100 pc using ground-based instruments with approximately $1''$ seeing. However, one of the main challenges in studying nearby galaxies lies in accurately determining their distances. Reliable distance determination methods, such as Cepheids and the tip of the red giant branch (TRGB), which offer accuracy within 5%, become difficult to employ beyond distances of 5 Mpc, as they necessitate to resolve individual stars (Jacoby et al., 1992).

Alternative methods like the Tully-Fisher relation (Freedman and Madore, 2010) and SNe II (Dessart and Hillier, 2005; Kasen and Woosley, 2009) suffer from larger uncertainties of approximately 20% and are commonly utilized for nearby galaxies. The [O III] λ5007 Å planetary nebula luminosity function (PNLF) presents a viable alternative approach for obtaining accurate distances with an error margin within 10% (Ciardullo et al., 1989; Jacoby, 1989; Jacoby et al., 1992; Ciardullo, 2010, 2013, 2022).

Planetary nebulae (PNe) are characterized by being ionized by low and intermediate mass stars, typically ranging from 1-8 $M_\odot$ in mass, during their evolution from the asymptotic giant branch to the white dwarf phase (Paczyński, 1971; Iben and Renzini, 1983). These PNe harbour central stars that emit high luminosity, surpassing $>$6000 $L_\odot$ (Vassiliadis and Wood, 1994), with around 12% of their total luminosity emitted in the [O III] λ5007 Å line (Dopita et al., 1992; Schönberner et al., 2007, 2010). This characteristic makes PNe relatively straightforward to detect in surveys targeting emission lines. Notably, the PNLF exhibits a distinctive exponential cutoff, rendering the brighter magnitude end of the luminosity function suitable as a "standard candle" (Jacoby, 1989; Ciardullo et al., 1989). Despite theoretical expectations of variations based on metallicity and age of the underlying stellar population (Dopita et al., 1992; Marigo et al., 2004), empirical evidence indicates that the PNLF remains consistent across different galaxy types, including elliptical, spiral, and irregular galaxies, which host diverse stellar populations (Ciardullo et al., 1989; Feldmeier et al., 1996, 1997).

Hence, the PNLF possesses a notable advantage as a distance indicator: the PNLF's bright-end cutoff M^* remains relatively constant regardless of variations in the local environment or galaxy

metallicity. This characteristic makes the PNLF applicable to both spiral and elliptical galaxies, offering an opportunity to test and compare other distance measurement methods. The potential of using PNe for distance measurements was recognized as early as 1978 by Jenner. Subsequently, Jacoby (1989) and Ciardullo et al. (1989) developed an empirical luminosity function known as the PNLF, which relies on the luminosity cutoff M^*. This pioneering work established the foundation for distance measurements using PNe, a method that continues to be employed. The PNLF has demonstrated its reliability and precision in obtaining distances to nearby galaxies within a range of approximately 20 Mpc with an accuracy better than 10 percent. Numerous studies have successfully utilized the PNLF in their research and observations (Ciardullo et al., 1993; Ferrarese et al., 2000; Ciardullo et al., 2002; Feldmeier et al., 2007a; Herrmann et al., 2008; Kreckel et al., 2017; Roth et al., 2021; Scheuermann et al., 2022).

Despite the advantages associated with the PNLF method, one of its primary challenges involves creating a comprehensive and reliable catalogue of PNe. While PNe can be relatively easy to detect due to their strong [O III] λ5007 emission, distinguishing them from other [O III]-emission objects, such as H II regions or SNR, can pose difficulties. In 1981, Baldwin et al. demonstrated that emission line ratios can serve as a means to differentiate PNe from other objects. Utilizing narrowband imaging, which combines an [O III] *on*-band filter, a wider *off*-band filter, and a filter centred around Hα, has proven effective in the identification of PNe.

In recent times, the field of PNLF distance measurements has undergone a significant transformation thanks to the introduction of advanced integral field unit (IFU) spectroscopy instruments. These instruments, exemplified by the Multi Unit Spectroscopic Explorer (MUSE), have brought about a revolution in the field by offering comprehensive spectral information across a wide field of view. This breakthrough has surmounted the limitations of narrowband imaging by enabling the detection of a greater number of PNe. The IFU spectroscopy technique allows researchers to effectively eliminate the strong stellar continuum in densely populated central regions, thus making it possible to detect PNe in previously inaccessible areas.

MUSE's optical integral-field spectrograph (IFS) (Bacon et al., 2010) is deployed on the 8.2 m Very Large Telescope (VLT) to facilitate such observations. (Roth et al., 2021) (Rot21) identify numerous improvements that MUSE contributes to, enhancing previous studies on the PNLF in various aspects:

- The VLT has a larger aperture, offering a collecting area four times larger than previous telescopes used in PNLF studies.
- MUSE provides a narrower effective bandpass, more than five times narrower than typical interference filters, reducing noise and improving the detectability and photometric accuracy of planetary nebulae in PNLF measurements.
- MUSE's spectral coverage from 4800 to 9300 Å and resolution of $R \sim 2000$ at 5000 Å allows the identification of contaminating objects like H II regions, SNR, and background galaxies, preventing them from affecting PNLF statistics.
- MUSE spectra enable the identification of spatial blends, allowing the separation of emission from merged sources such as PNe pairs.
- Unlike narrowband filters, MUSE does not introduce photometric errors dependent on the velocity of emission-line objects, providing consistent photometric throughput for all PNe regardless of their velocity.

Earlier investigations into the PNLF heavily relied on narrow-band imaging, which suffered from significant contamination by the host galaxy's background stellar continuum emission. Consequently, the majority of the PNe identified in these surveys were predominantly found at larger galactocentric radius (Herrmann et al., 2008). This location choice minimizes contamination but also results in lower PNe density, which correlates with stellar surface density (Ciardullo et al., 1989). The utilization of optical integral field spectroscopy (IFS), on the other hand, offers complete spectral information, enabling precise fitting and removal of the stellar continuum. Previous studies have already demon-

strated the effectiveness of IFS in providing accurate spectrophotometry of point sources, including PNe (Arribas et al., 1998; Sil'chenko and Afanasiev, 2000; Roth et al., 2004, 2005).

In star-forming spiral galaxies, the use of this technique enables the modelling and removal of background line emissions originating from unresolved stars and the diffuse interstellar medium (Kreckel et al., 2016). It allows for the simultaneous observation of various bright emission lines, such as Hα, [N II] λ6584 Å, and [S II] $\lambda\lambda$6717,6737 Å. These emission lines can be utilized to differentiate PNe from other [O III] emitters like H II regions and SNR (Sabbadin et al., 1977; Baldwin et al., 1981; Blair and Long, 2004; Riesgo and López, 2006; Kreckel et al., 2017). Previous studies employing IFUs have demonstrated the viability of this method in extracting line fluxes from PNe (Roth et al., 2004; Sarzi et al., 2011). Nevertheless, the aforementioned studies faced limitations due to their restricted field of view and the limited number of observed PNe. In contrast, modern IFU surveys of nearby galaxies have been intentionally designed to track star formation with enhanced depth and spatial resolution, resulting in the detection of a larger population of PNe. As a consequence, there have been significant advancements in the accuracy of distance estimates for these galaxies.

MUSE's IFS, with its relatively large field of view of approximately 1 arcmin^2, overcomes the limitations of previous narrowband imaging techniques. For example, Kreckel et al. (2017) utilized MUSE to identify 63 PNe in a specific region of the face-on spiral galaxy NGC 628, employing approximately 45-minute exposures. The derived PNLF distance from this study slightly differed from distances obtained using narrowband filters in previous works. This discrepancy was attributed to MUSE's enhanced capability to distinguish between PNe and SNR. In more recent research, Roth et al. (2021) and Scheuermann et al. (2022) obtained PNLF-based distances to galaxies beyond the 20 Mpc range, while demonstrating the reliable measurement of distances to late-type galaxies. These advancements extend the calibration of Type Ia supernovae beyond the previous work conducted by Feldmeier et al. (2007a).

We conducted an examination of most of the disc region of the nearby grand design spiral galaxy NGC 628. We utilized IFU spectroscopy obtained with the VLT-MUSE (Kreckel et al., 2016). The nearly face-on orientation of NGC 628 ($i = 9°$, Blanc et al. (2013)) minimizes the contamination of PNe by other objects, while reducing the impact of internal dust extinction on the observations. NGC 628 exhibits a well-documented metallicity gradient described by 12 + log(O/H) = 8.834–0.485×R (dex R_{25}^{-1}), derived from direct abundance measurements of auroral lines that are sensitive to temperature (Berg et al., 2015). Within the central region ($R < R_{25}$), the galaxy displays roughly solar abundances (Asplund et al., 2009). However, the distance to NGC 628 remains uncertain, with estimates ranging from 7 to 10 Mpc, as determined by various techniques.

1.1 PNe Working Definition

The definition of a PNe has been a subject of controversy, with differing classification criteria that has evolved since their discovery two centuries ago. The term "PNe" is argued to possess a specific physical or evolutionary significance, referring to the ionized gaseous shell expelled during the late stages of the asymptotic giant branch (AGB) phase. However, reaching a consensus on a taxonomic definition for PNe remains challenging. In a comprehensive analysis of the literature and extensive census of PNe, Frew and Parker (2010) proposed the following observational and physical characteristics to define a PNe:

- Characterized by a round or axisymmetric morphology, these objects occasionally exhibit multiple shells or haloes.
- Photoionized emission-line spectrum, including hydrogen, helium, and heavier elements.
- De-reddened Hα surface brightness between log S(Hα)=+0.5 and -6.5 erg cm^{-2} s^{-1} sr^{-1}.
- Reddening-corrected [O III] absolute magnitude, $M_{[\mathrm{O\ III}]}$, between -4.5 and +6.0 mag.
- The radio spectrum reveals thermal free-free emission.

- Presence of cool dust in the infrared and occasionally PAH emission.
- Nebular radius $\leq$2.5 pc, with most falling below 1.5 pc.
- Ionized mass roughly between 0.005 and 3$M_\odot$, with a median value of 0.5$M_\odot$.
- Electron density between 100 and 10^5 cm^{-3}.
- Typically, the expansion velocity of the shells lies between 10 and 60 km s^{-1}.

A PNe surrounds a central star which is a hot, low-mass object with a minimum temperature of 20.000K and a mass between $\sim$0.55 and 0.9$M_\odot$. The star's observed absolute visual magnitudes range from -2.5 to +7.5, surface gravities range from log (g) 2.5 to 7.5 cm s^{-2}, and most have spectral types ranging from OB and sdO to DAO and DA.

1.2 PNe Detection Techniques

Various techniques have been utilized to discover PNe due to the wide array of characteristics exhibited by these objects, including apparent size, morphology, flux, surface brightness, excitation class, central star luminosity, and evolutionary state. Pioneering observers such as Charles Messier and William Herschel identified some of the brightest and most famous PNe more than two centuries ago, directly observing them through telescopes. Herschel, in particular, classified nebulous objects as PNe solely based on their morphological characteristics. Various methods have been used to discover PNe over the last hundred years, notably: spectroscopic discoveries, image comparison techniques, visual inspection of optical imagery, or discoveries at non-optical wavelengths.

1.3 Rise, Fall and Rebirth of the PNLF

During the late 1980s, a remarkable discovery emerged when it was found that the PNLF of [O III] λ5007 could serve as a precise extragalactic standard candle. Despite the absence of a solid theoretical explanation, this method successfully withstood numerous internal and external tests. The PNLF technique has established itself as a reliable method for estimating distances to large galaxies within a range of about 20 Mpc. Between 1989 and 2010, there was significant research interest in measuring and modelling the PNLFs of distant galaxies, with almost a hundred publications dedicated to the topic. However, in the following decade, the number of papers declined to less than 30, mostly focusing on identifying faint planetary nebulae in Local Group galaxies. This decline can be attributed to several reasons.

Firstly, the landscape of cosmology changed by 2012, with the aim of reducing uncertainties associated with the Hubble constant. To achieve this, it became crucial to minimize errors in zero-point calibration for each method used. Consequently, the approach to determining the Hubble constant shifted away from relying on intermediate-distance standard candles, such as the PNLF, and instead directed their attention towards the distance scale of the Milky Way and the parent galaxies of Type Ia SN. This two-step approach bypassed the utilization of PNLF, as it aimed to minimize uncertainties in zero-point calibration for each distance measurement method. Furthermore, the calibration of PNLF posed challenges due to the lack of a robust theory or local calibration for the expected absolute magnitude of the PNLF cutoff M^*. Consequently, modern distance ladders were developed with the aim of circumventing this additional uncertainty (Ciardullo, 2022).

The decreased utilization of PNLF was also influenced by the identification of possible systematic errors. While PNLF distances showed satisfactory agreement with those obtained from the Cepheid period-luminosity relation up to a distance of approximately 10 Mpc, a noticeable offset began to emerge beyond this limit. Notably, the PNLF distances to elliptical galaxies in the Virgo and Fornax clusters were approximately 0.2 magnitudes shorter compared to the Cepheid distances to spiral galaxies within the same systems. This offset was also observed when comparing with the surface brightness fluctuation (SBF) method. Consequently, the PNLF could not be reliably extended to the

distances required for calibrating the upper rungs of the distance ladder (Ciardullo, 2022). The issue of "overluminous" objects further complicated PNLF studies. Initially, these objects challenged the assumptions about the shape of the PNLF. Subsequently, it was discovered that the identified bright [O III] emitters could be attributed to either foreground PNe within their presumed host galaxy or background galaxies exhibiting Lyα emission that was shifted into the narrow-band filter's bandpass used for their initial detection.

Lastly, technological limitations also played a role. The first wave of PNLF measurements utilized 4m class telescopes with narrow interference filters. However, the introduction of 8m class telescopes brought new challenges. The telescope imagers used in these observations were specifically designed for wider fields of view and faster scanning, leading to an increase in the full width at half-maximum of the filters' bandpasses. Moreover, the expense associated with acquiring redshifted narrow-band interference filters for [O III] and Hα became excessively high. Therefore, the benefits of larger collecting areas were offset by the increased sky background resulting from wider-bandpass filters. Consequently, the enhancements in PNLF distance measurements were only modest improvements rather than significant breakthroughs.

Recently, the introduction of IFU spectrographs on 8m class telescopes has significantly enhanced the prospects for PNLF surveys. Compared to traditional narrow-band imaging, IFU spectroscopy offers several advantages. It allows for immediate identification and exclusion of unwanted contaminants in PNe samples through spectral classification. Additionally, the effective bandpass of the IFU spectrograph is approximately five times narrower compared to conventional interference filters, leading to more precise PNe detections. Due to the limitations imposed by background noise in extragalactic PNe observations, the emission-line signals exhibit considerably higher contrast compared to the continuum. This characteristic leads to a significant improvement in the signal-to-noise ratio, exceeding a twofold increase. Additionally, when combined with larger telescope apertures, the IFU spectrograph transforms the PNLF from a specialized technique on the distance ladder into a valuable tool for investigating distances that are pertinent to cosmological research.

The remarkable impact of IFUs in advancing PNLF studies is exemplified by the MUSE IFU spectrograph installed on the European Southern Observatory (ESO) VLT. Despite its relatively limited field-of-view, MUSE offers exceptional image quality, spectral resolution, and wavelength coverage, enabling unprecedented exploration of PNLF research. Through the combined capabilities of MUSE and VLT, researchers have successfully identified PNe in various nearby galaxies, encompassing both spiral and elliptical types, and have consistently measured PNLFs within a range of approximately 20 Mpc. Furthermore, the incorporation of a differential emission-line filter (DELF), which allows for *on*-band/*off*-band image subtraction, has enabled accurate PNLF surveys up to approximately 40 Mpc. This technique minimizes fixed-pattern noise resulting from flatfield corrections.

By employing dedicated ground-layer adaptive optics observations, it becomes possible to derive PNLF distances to galaxies reaching approximately 40 Mpc, with a statistical error of approximately 5%. This distance holds cosmological significance as it offers a means to address the "tension" observed between locally measured values of the Hubble constant and those derived from the cosmic microwave background (Giovanelli et al., 1998; Tonry et al., 2000; Freedman, 2021; Roth et al., 2021). Theoretically, PNLF measurements from surveys conducted in a dozen galaxies at a distance of around 40 Mpc, each with a typical statistical uncertainty of about 5%, could contribute to reducing the overall (random) error associated with the Hubble constant to approximately 3% (Ciardullo, 2022). As a result, PNLF measurements have the potential to contribute towards exploring and potentially resolving the current disparities between local measurements of H0 and those derived from the microwave background, thus aiding in alleviating the existing tension.

This work aims to demonstrate the effectiveness of MUSE in improving distance estimates to NGC 628, a galaxy previously studied using alternative methods. In Section 2, we present the data that is used for this study and in Section 3 we describe the methods used in this study. In Sections 4 and 5 we present and discuss the results. We conclude in Section 6.

Chapter 2

Data

NGC 628

NGC 628, also known as M74, is a prominent spiral galaxy categorized as SA(s)c. Over the past two decades, it has witnessed the occurrence of two Type II supernovae (SN 2003gd and SN 2013ej) and one Type Ic supernova (SN 2002ap). This galaxy stands out as the largest and brightest member within its group, spanning an expansive area of approximately $12'$ in the sky. Notably, NGC 628 presents an almost face-on orientation, with an inclination angle estimated to be around 9 degrees according to (Lang et al., 2020), which helps minimize the contamination of PNe by other objects and mitigates the influence of internal dust extinction on the observations. However, the presence of numerous compact H II regions and SNR poses a significant challenge during the PNe identification process. The systemic velocity of NGC 628 is approximately 657 km/s based on (Lu et al., 1993), and due to its nearly face-on perspective, the velocities of PNe in the galaxy exhibit a relatively narrow distribution. The velocity dispersion of PNe ranges from approximately 50 km/s in the central arcminute to less than 15 km/s at distances corresponding to the disk scale lengths (Herrmann and Ciardullo, 2009). Figure 2.1 illustrates a white-light image of NGC 628. The observations were conducted using the MUSE instrument, as detailed in Bacon et al. (2014). The instrument is located at the Nasmyth focus of the UT4 8.2m telescope situated at the VLT observatory of the ESO in Chile. To capture the data, all observations were carried out in the extended mode, which encompasses the wavelength range of 4800-9300 Å. The resolution was approximately 1800-3600, with a dispersion of 1.25 Å per pixel. The resulting data cubes were generated using the standard sampling of $0''.2$ x $0''.2$ x 1.25 Å. It should be noted that the wide-field mode of MUSE covers a field of view measuring 1×1 arcmin^2, capturing only a portion of the target galaxy. In order to adequately sample the majority of the star-forming disc, twelve different pointings were taken.

The MUSE data cubes used in this study were sourced from multiple programs conducted at the VLT during the period from 2016 to 2019. As a result, the data exhibit heterogeneity and cover a wide range of observing conditions. The recorded measurements include seeing values ranging from $0''.65$ to $1''.1$ and exposure times varying between 2530 and 2970 s (refer to Table 2.1 for details). Assuming a typical seeing value of $0''.8$ across all fields and considering the reported distance range for the galaxy, the achieved spatial resolution is estimated to be approximately 30-50 pc. We retrieved

Table 2.1: Observational conditions for NGC 628 from ESO Archive (Roth et al., 2021): "clouds": some clouds registered during the night, "clouds*": clouds passing during an exposure.

Pointing	K1	K2	P1	P2	P3a	P3b	P4	P5	P6	P7	P8	P9	P12
Seeing	$0''.77$	$0''.83$	$0''.76$	$1''.14$	$1''.49$	$0''.95$	$1''.08$	$1''.05$	$0''.69$	$0''.70$	$0''.82$	$0''.96$	$0''.72$
Weather	clear	clear	clear	clouds	clear	clouds	clear	clouds	clouds	clouds	clouds*	clouds*	clouds*
T (s)	2535	2535	2970	2970	2970	2970	2970	2970	2970	2970	2970	2970	2970

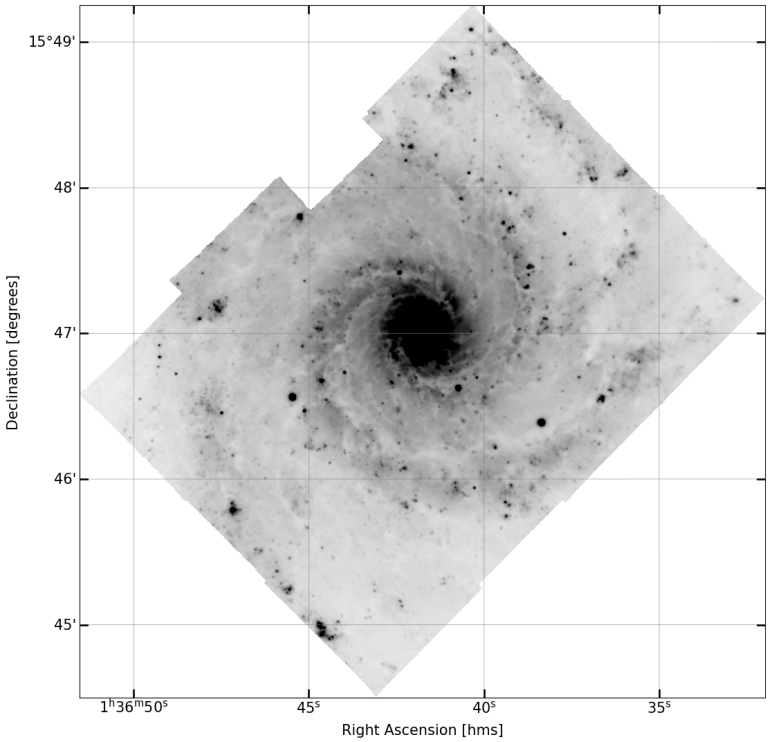

Figure 2.1: White-light image of NGC 628. Pixel values normalized with IRAF's zscale algorithm to facilitate the visualization.

the publicly available and fully reduced (and mosaicked) MUSE data cube from the ESO archive (Romaniello et al., 2018). The data reduction was performed by Roth et al. (2021) (Rot21) who used MUSE data reduction software (DRS) by Weilbacher et al. (2020). Figure 2.2 (Roth et al., 2021, Figure 24, p. 24) displays the 12 pointings recorded in the MUSE archive. The analysis conducted by Kreckel et al. (2017) (Kre17) concentrated on three specific pointings, which yielded a total of 63 identified PNe. Among these pointings, the P3 field was observed on two separate occasions, capturing different epochs and distinct observing conditions.

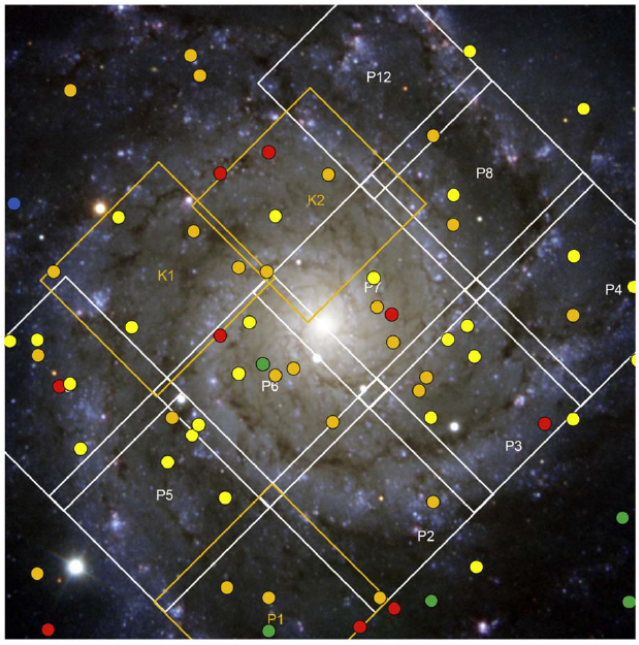

Figure 2.2: NGC 628 observations using MUSE conducted by Kreckel et al. (program 094.C-0623), who designated the pointings as K1 and K2. Blanc et al. (program 098.C-0484) also contributed to the observations with pointings labelled as P1 through P12. The pointings are depicted as orange and white squares, respectively. From Roth et al. (2021, Figure 24, p. 24).

Traditional PNLF measurements were typically conducted using direct imaging cameras equipped with narrowband filters, primarily on 4m class telescopes' prime focus. In order to explore the potential and constraints of using IFS for PNLF distance calculations, the images presented in this paper are derived from MUSE data cubes.

Chapter 3

Methodology

Previous work has discovered extragalactic PNe, some of them using MUSE data cubes. Hermann et al. (2008) (Her08) did a narrowband PNLF study of NGC 628 identified 153 PNe [1] , while Kre17 found 63 PNe in K1, K2 and P1. More recently, Rot21 and Scheuermann et al. (2022) (Sch22) also obtained PNLF-based distances to NGC 628 after the identification of 202 and 139 PNe, respectively. To the best of our knowledge, these are the four studies that have used the PNLF method to derive the distance to NGC 628, and have guided our approach.

Our initial sample of PNe candidates were selected by observing unresolved objects in the maps of the [O III] emission line. Nevertheless, it is crucial to eliminate contamination from other objects that exhibit different line-strength ratios, such as H II regions and SNR. This ensures an accurate fitting of the PNLF and enables us to determine the distance to the galaxy.

3.1 Differential Emission Line Filtering (DELF)

The detection of PNe is a challenging task due to the dominant presence of the host galaxy's continuum surface brightness in broadband images. To overcome this challenge, the PNLF distance technique utilizes narrow-band filters that suppress most of the continuum while allowing the transmission of light within a specific wavelength range, typically targeting the [O III] λ5007 emission line of PNe. Jacoby (1989) (Jac89) introduced the *on*-band/*off*-band technique, which entails deducting a proportionally adjusted *off*-band continuum image from a corresponding [O III] *on*-band image in order to effectively eliminate the continuum surface brightness. By applying this technique, PNe appear as faint point sources against a flat noise floor.

Building upon the *on*-band/*off*-band technique, Rot21 further refined the method by creating stacks of data cube layers centred around the wavelength of the Doppler-shifted [O III] line. Roth et al. (2018) showed that MUSE data cubes have the potential to implement synthetically the *on*-band/*off*-band technique. By combining the data cube layers within a few wavelength bins centred around the Doppler-shifted [O III] emission line and comparing them to an appropriate *off*-band image, a substantial reduction in the effective filter bandwidth, decreasing it from the range of 30 to 50 Å to as low as 4 or 5 Å, is made possible (see the 20 Å-wide narrow-band Figure 3.1). Consequently, this reduction in bandwidth diminishes the photon shot-noise contribution from the host galaxy, resulting in an improved signal-to-noise ratio of PNe detections by a factor of approximately 2.5. Additionally, the use of IFUs allows for a spaxel-to-spaxel approach to flux calibration, which further enhances the precision of PNe photometry.

[1] In previous studies of the PNLF, such as the one conducted by Her08, narrow-band imaging was utilized. However, this method is prone to significant contamination from the background stellar continuum emission of the galaxy. Consequently, the majority of the identified PNe in these surveys were situated at larger radii where the contamination is diminished, but the density of PNe (which corresponds to the density of stars) is lower (Ciardullo et al., 1989).

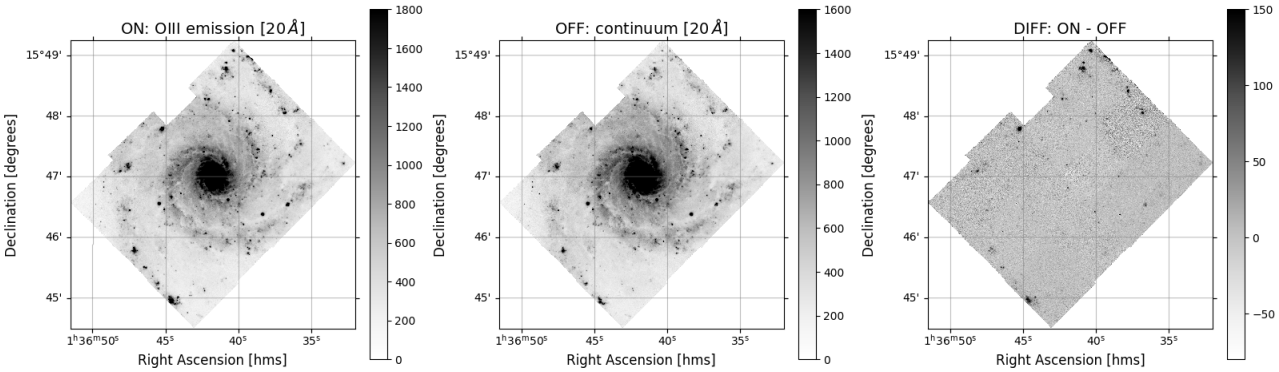

Figure 3.1: Narrow-band (20 Å) images. Left: "*on*" image, centred on the Doppler-shifted [O III] 5007 line. Middle: "*off*" (continuum) image, covering the Doppler-shifted [5040-5060] Å range. Right: "*diff*" image (*on* - *off*). Pixel values normalized with IRAF's zscale algorithm to facilitate the visualization.

Following Rot21, we have created stacks of 15 single data cube layers, each with a width of 1.25 Å. These stacks are centred around the wavelength of the Doppler-shifted [O III] line, accounting for a range of PNe radial velocities within ±500 km/s centred on the galaxy's systemic velocity. Furthermore, we generated a 122.5 Å intermediate-bandwidth *off* continuum image by combining 99 data cube layers located redward of the redshifted $\lambda_0 = 5007$ Å emission line ($\lambda_z = 5017.5$ Å), covering the wavelength range [5043.75 - 5166.25] Å. From each of the 15 *on* layers, we subtract the normalized (1/99) continuum *off* image, resulting in a total of 15 *diff* images.

In line with the methodology employed by Rot21, we have generated stacks comprising 15 individual data cube layers, each with a width of 1.25 Å. These stacks are centred around the wavelength of the Doppler-shifted [O III] line, encompassing PNe radial velocities within a range of ±500 km/s, centred on the systemic velocity of the galaxy. Additionally, we produced an intermediate-bandwidth continuum image spanning 122.5 Å. This image was created by combining 99 data cube layers located beyond the redshifted emission line at $\lambda_0 = 5007$ Å ($\lambda_z = 5017.5$ Å), covering the wavelength range of [5043.75 - 5166.25] Å. Subsequently, we subtracted the normalized continuum *off* image from each of the 15 *on* layers, resulting in a total of 15 *diff* images. [2] The MUSE instrument pos-

Unbinned Image #	Layer (#)	Wavelength (A)	Radial Velocity (km/s)	Coadded Image (#)
1	247	5008,75	105,9	
2	248	5010,00	180,6	-
3	249	5011,25	255,3	-
4	250	5012,50	329,9	-
5	251	5013,75	404,6	1
6	252	5015,00	479,3	2
7	253	5016,25	554,0	3
8	254	5017,50	628,7	4
9	255	5018,75	703,4	5
10	256	5020,00	778,1	6
11	257	5021,25	852,7	7
12	258	5022,50	927,4	-
13	259	5023,75	1002,1	-
14	260	5025,00	1076,8	-
15	261	5026,25	1151,5	

Figure 3.2: Data cube layers and corresponding narrow-band images for NGC 628. Each layer (bin) has a width of 1.25 Å, and the narrow-band images used for PNe detection consist of three consecutive layers. Only the central seven coadded frames will be used for PNe identification.

sesses a wavelength resolution that spans approximately two spectral elements within the data cubes.

[2] A similar approach will be followed with other important emission lines such as Hα, [N II] or the doublet [S II], which aid in the reliable classification of PNe.

Consequently, the [O III] λ5007 emission from a PNe is typically distributed across two or three adjacent wavelength bins in the data cube. This validates our approach of considering three neighbouring spectral bins when detecting PNe. Therefore, Our method for detecting PNe consists of combining the [O III] flux from three neighbouring layers within the cube.

Figure 3.2 depicts the procedure described above. The shaded row in grey represents the 254th wavelength bin, which corresponds to the systemic velocity of the galaxy at 657 km/s. The individual PNe within the galaxy exhibit internal motions that cause their 5007 Å emission to shift to different wavelengths, ranging from approximately 5030 Å (wavelength bin 247) to 5045 Å (wavelength bin 261) depending on their velocities. The red and blue bars in the figure demonstrate that by combining three consecutive layers of the data cube, we generate 13 coadded images with effective bandpasses of 3.75 Å. This consolidation enables us to capture the complete [O III] emission from all the PNe while significantly improving the contrast between the PNe and the continuum. As a result, very faint emission-line objects become detectable compared to a narrowband image with a larger bandwidth (e.g., 40 Å). To be noted, we use only the 7 central coadded frames to identify PNe due to the too large deviations of the planetary candidates detected in the three outermost frames with respect to the galaxy's systemic velocity.

To summarize, the DELF technique, as an extension of the traditional *on*-band/*off*-band technique to MUSE data cubes, offers several advantages. It allows for narrower filter bandwidths, reducing the background flux from the host galaxy, while minimizing spaxel-to-spaxel flat-field residuals, particularly problematic in regions characterized by high host galaxy surface brightness. These advantages enable more accurate PNLF studies and expand their applicability to much greater distances compared to previous investigations.

3.2 Source Detection and Photometry

In terms of source detection and photometry, our procedure involved multiple steps. Firstly, we conducted a search for unresolved objects in the 7 coadded *diff* [O III] image maps. Subsequently, we measured their fluxes using aperture photometry while subtracting the background within a surrounding annulus. Last, we accounted for an aperture correction and for Milky Way extinction, and converted the fluxes to apparent magnitudes.

3.2.1 Step 1: Source Identification

We employed the PHOTUTILS Python package (Bradley et al., 2019) for source identification. This package incorporates the DAOPHOT algorithm developed by Stetson (1987). Despite slight variations in seeing and weather conditions across the pointings (refer to Table 2.1), we opted to apply the search algorithm to the entire mosaic simultaneously. Specifically, the noise level was estimated using iterative three-sigma clipping based on the standard deviation. Subsequently, we conducted a search for objects surpassing a threshold of 3.5 times the estimated noise level, and with a FWHM set to 5.0 pixels (corresponding to $1''$ or slightly above the average seeing across all pointings). We also obtained the sources' centroids from the brightest *diff* image in the series. This constituted our preliminary catalogue of PNe candidates.

We excluded sources positioned near the borders and followed a similar criterion as in Rot21, i.e. only considered PNe candidates if they appeared in a minimum of three consecutive *diff* frames and displayed a point-source morphology. Also, sources with the maximum peak flux in either the first three or last three coadded *diff* images were removed from the sample because of a too large deviation from the galaxy's systemic velocity, resulting in 7 effective (out of the 13) coadded *diff* images. This analysis resulted in 9312 sources found in the seven *diff* images. As an example, the PNe candidates found in the central (i.e. at the galaxy's systemic velocity) coadded image are shown in Figure 3.3 (this is the image where most sources were found). Figure 3.4 shows the sources found in the seven

diff images where they are identified.[3] After identifying those sources with similar centroids such

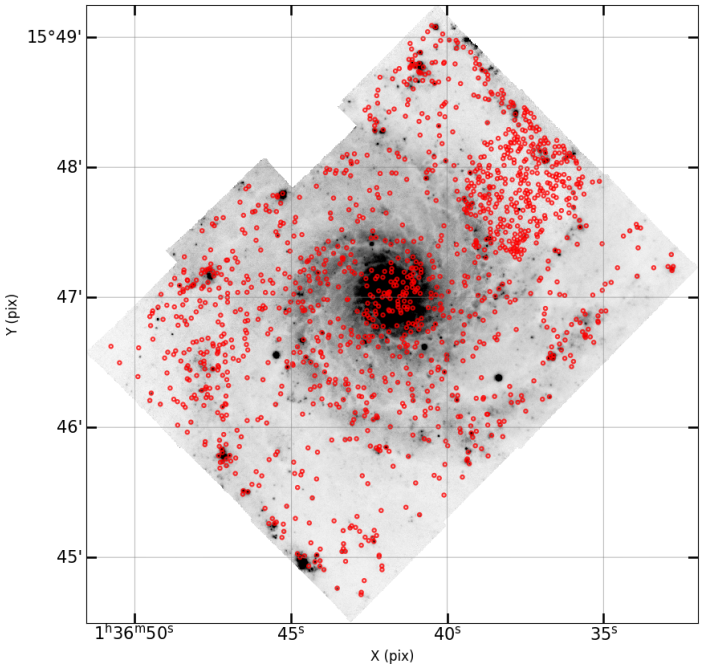

Figure 3.3: Sources identified with PHOTUTILS's DAOPHOT algorithm in the (central, 4th) 3-bin coadded *diff* image. The background image is a narrowband (20 Å) *on* (emission) [O III] image.

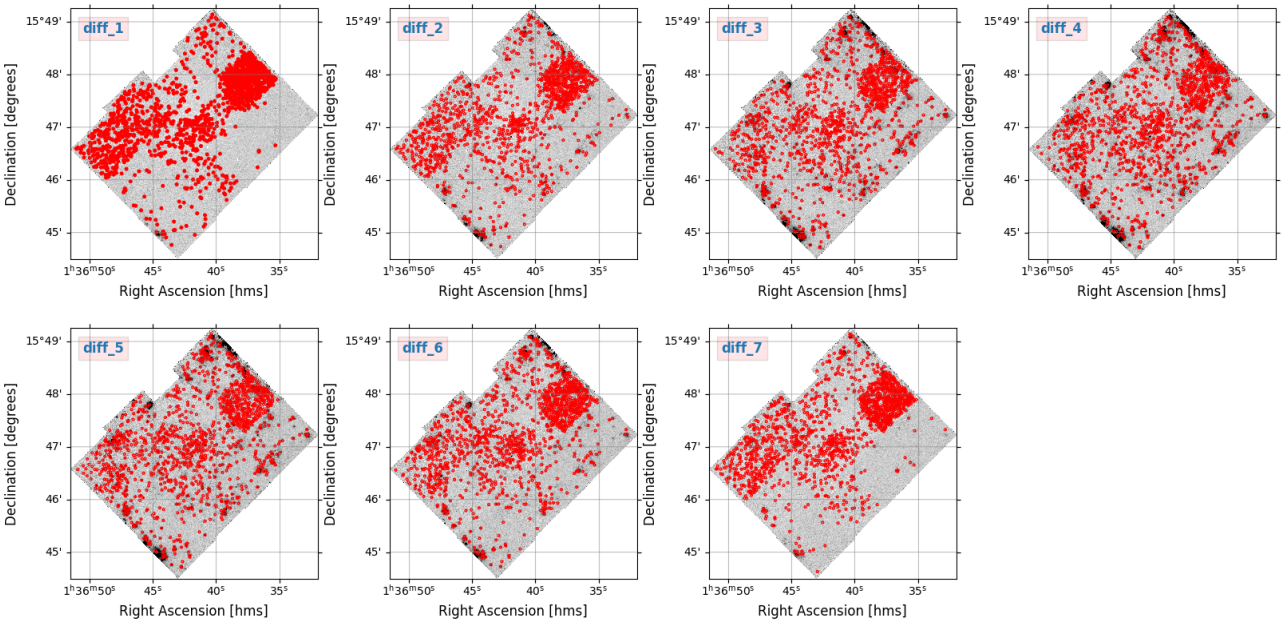

Figure 3.4: 9312 sources identified in total with PHOTUTILS's DAOPHOT algorithm in each of the seven 3-bin coadded *diff* images. The background images are the coadded *diff* images. Intensity scale normalized to same limits (see right-hand side bar) across all the images to facilitate visualization.

that they could be considered the same source, ensuring they appear in at least three consecutive *diff* images, and don't deviate too much from the galaxy's systemic velocity, our initial PNe sample had 1009 PNe candidates with the centroids taken from the coadded *diff* image with the maximum peak flux. The number of candidates over the seven coadded *diff* images is shown in Table 3.1 and the corresponding locations in Figure 3.5. As it can be seen, most of the sources are found in the central 7th (i.e. at the galaxy's systemic velocity) and 8th coadded *diff* images.

[3]Most of them appearing in various *diff* images.

Table 3.1: PNe candidates identified in the seven coadded *diff* images.

diff image	1	2	3	4	5	6	7
Number PNe candidates	60	47	76	522	199	53	52

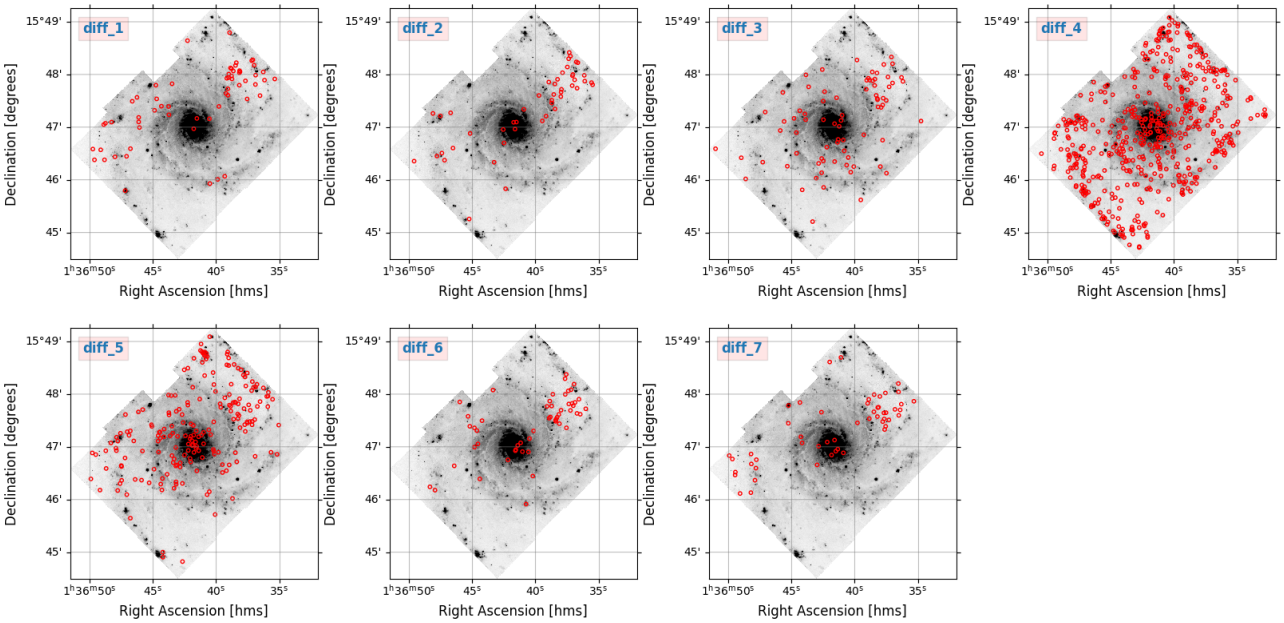

Figure 3.5: Initial sample of PNe candidates: sources are shown in the coadded *diff* image where they have the maximum peak flux. Background image is the same narrowband (20 Å) *on* (emission) [O III] image to facilitate the localization of the candidates.

3.2.2 Step 2: Aperture Photometry

Next, we conducted aperture photometry in the fifteen unbinned (1-layer) *diff* images. This process created a short spectrum comprising fifteen layers in the relevant wavelength region. Despite some observational differences among pointings, we chose a common aperture radius of 3 pixels (approximately the median seeing 0.″73 across the twelve pointings). The inner and outer sky annulus were set at 12 and 15 spaxels, respectively.

Using a small aperture size has proven to be beneficial in maximizing the signal-to-noise ratio by capturing the brightest region of the object (Howell, 1989). Instead, careful attention was given to compensating for the flux lost beyond the source's aperture. To eliminate bright contaminants within the annulus, an iterative three-sigma clipping process was employed. The median of the annulus (after sigma clipping) was scaled to match the size of the central aperture and subsequently subtracted.

It must be noted a couple of limitations related to these photometric calculations. First, unfavourable weather conditions had a significant impact on the majority of the MUSE observations of NGC 628, as indicated by the ESO archive and illustrated in Table 2.1. Second, the lack of suitable point sources in all the fields posed a challenge in identifying foreground stars for aperture correction measurements, with notable differences observed among the point-source candidates in each field. The aperture corrections, later explained and which represent the primary source of uncertainty in our photometry, were derived by obtaining the [O III] radial profile for nine isolated *point sources* found across the whole mosaic. We ignored the potential dependency on wavelength and applied the same correction to other lines.

3.2.3 Step 3: Short Spectrums

In the third step, the [O III] flux was measured by fitting a one-dimensional Gaussian profile to the 15-bin short spectrums. The central wavelength, the sigma (or full width at half maximum FWHM), and constant level were left as free parameters in the fit, with the constraint that the sigma had to be larger than 1.25 Å. In almost all cases, most of the integrated flux over the 15-bin fitted profile was accounted for by adding the fluxes in the central five bins around the peak of the Gaussian fit. The majority of the fits seemed well-behaved, without almost any cases of double-lined or broadened profiles (arising from overlapping PNe with different radial velocities), automatically identifiable by an anomalously large sigma estimate.

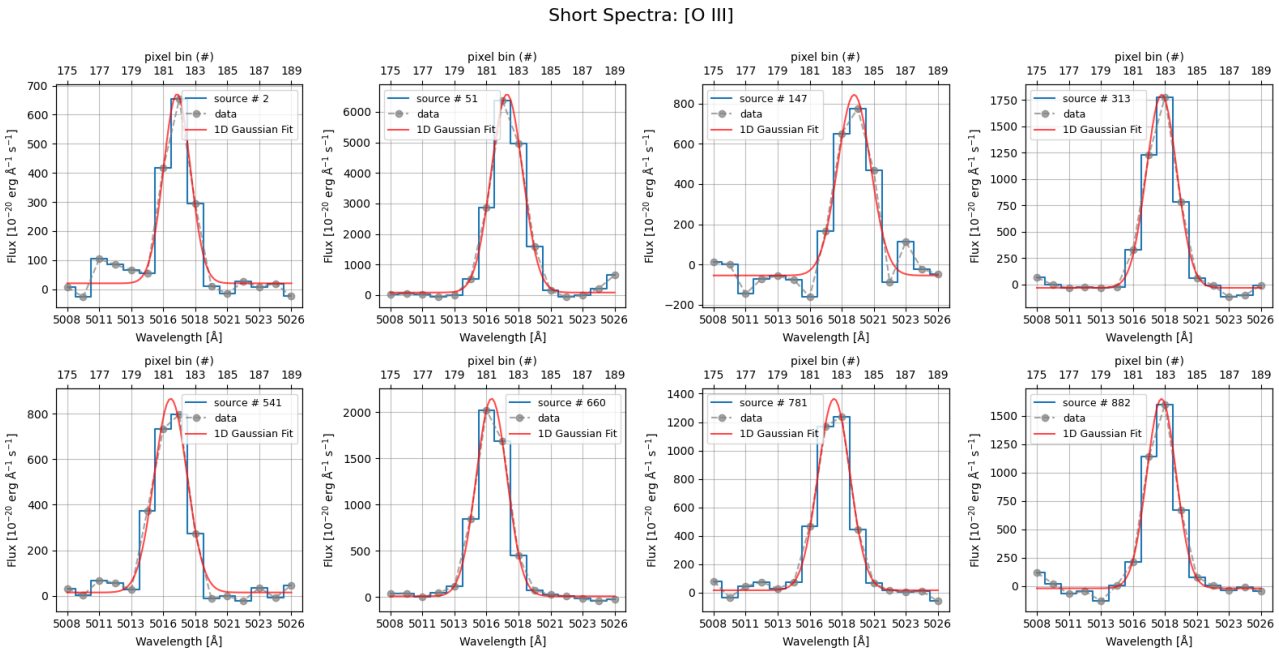

Figure 3.6: 15-bin short spectra and 1D Gaussian fits for a sample of PNe candidates.

The same approach was taken with five other emission lines that will be used to remove contaminants from our PNe candidates sample, namely: Hβ λ4861.33, Hα λ6562.82, [N II] λ6583.46, and [S II] $\lambda\lambda$6716.44, 6730.81 [4] . In all cases, a continuum was estimated by coadding 49 x 2 layers to the blue/red sides of the line of interest and subtracting it from the 15 *on* images after proper scaling. Figure 3.6 shows some examples of [O III] fits for a few random PNe candidates. Figures 3.7 and 3.8 show the relevant regions for the *on* and *off* (continuum background) images, while Table 3.2 show the relevant wavelengths.

Table 3.2: Wavelength ranges for the *on* and *off* (blue and red) images.

Emission Line	Doppler-shifted	"On" Range	"Off" Range (blue)	"Off" Range (red)
Hβ	4872.50	4863.25-4881.25	4792.50-4852.50	4892.50-4952.50
[O III] λ5007.00	5017.50	5008.75-5026.25	4890.00-4950.00	5037.50-5097.50
Hα	6577.50	6568.75-6586.25	6482.50-6542.50	6617.50-6677.50
[N II] λ6583.46	6597.50	6588.75-6606.25	6482.50-6542.50	6617.50-6677.50
[S II] λ6716.44	6731.25	6722.50-6740.00	6651.25-6711.25	6765.00-6825.00
[S II] λ6730.81	6745.00	6736.25-6753.75	6651.25-6711.25	6765.00-6825.00

[4] We also analysed [O III] λ4958.91, [N II] λ6548.05, and [O I] λ6300.30.

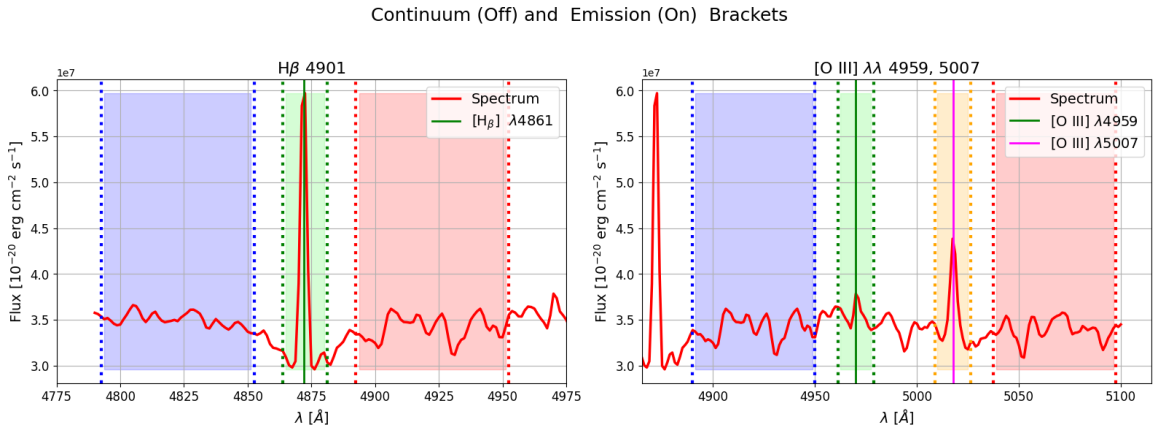

Figure 3.7: Continuum (*off*) and emission (*on*) bin ranges. Left: Hβ. Right: [S II] $\lambda\lambda$ 6716.44, 6730.81. 15 bins and 2 x 49 bins (2 x 60 Å) are used for the *on* and the continuum *off* ranges, respectively. Each of the 15 *on* images were continuum-subtracted (*off* image scaled by 1 / (2 x 49)) to obtain the 15 *diff* images, where aperture photometry was carried out.

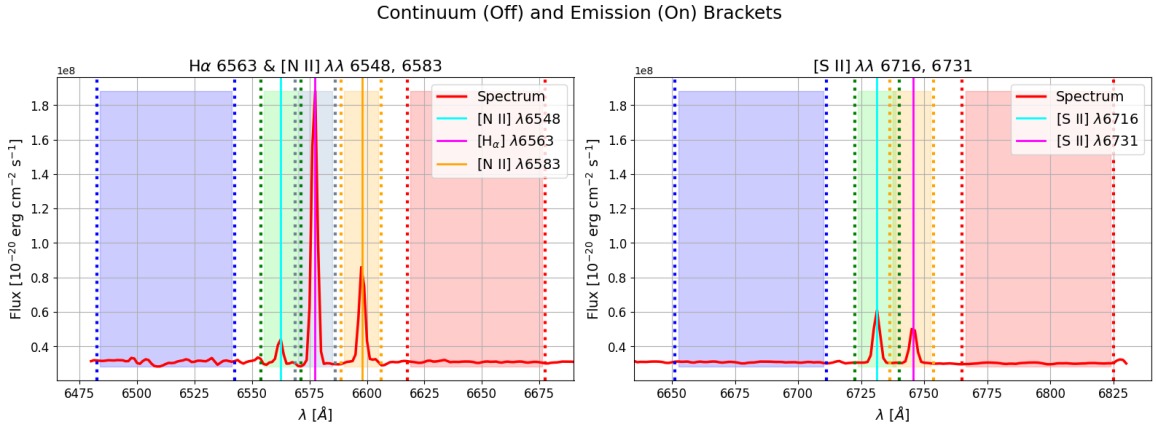

Figure 3.8: Continuum (*off*) and emission (on) bin ranges. Left: [N II] $\lambda\lambda$6548.05, 6583.46 and Hα. Right: [S II] $\lambda\lambda$ 6716.44, 6730.81. 15 bins and 2 x 49 bins (2 x 60 Å) are used for the *on* and the continuum *off* ranges, respectively. Each of the 15 *on* bins were continuum-subtracted (*off* image scaled by 1 / (2 x 49)) to obtain the 15 *diff* images, where aperture photometry was carried out.

3.2.4 Step 4: Aperture Correction

In order to account for the flux beyond the 3-pixel measuring aperture, we implemented an aperture correction technique by utilizing point sources within the field. Related literature has reported that due to the small field of view of MUSE it often resulted in insufficient bright stars in galaxy exposures from the ESO archive to reliably measure the PSF using the data layers of interest. Additionally, distinguishing foreground stars from semi-resolved globular clusters within a nearby galaxy has proven to be a challenging task. Therefore, different approaches have been implemented for the determination of the aperture correction.

To address this challenge, we generated broadband images with a width of 200 Å by coadding 160 data cube layers on the red side of the [O III] line. We used once again the DAOPHOT algorithm to identify point-source candidates that were sufficiently bright. The 50 brightest point sources across the 12 fields were selected and, among these, we visually identified those that were "isolated" (see Figure 3.9). For point sources that exhibited well-behaved characteristics, we conducted aperture photometry at various radii ranging from $R = 0.5$ to $R = 12.0$ pixels, with incremental steps of 0.5 pixels. The sky annulus used for these measurements had fixed inner and outer radii of 12 and 15 pixels, respectively. The median of the ratios between the flux within 3 pixels and the asymptotic value at a very large radii for the 9 point sources identified was adopted as the aperture correction

(see Figure 3.10), with the caveat that (i) this correction was not particularized for each of the twelve fields, and (ii) we ignored any wavelength dependency, as we applied the same correction to the other five lines under study.

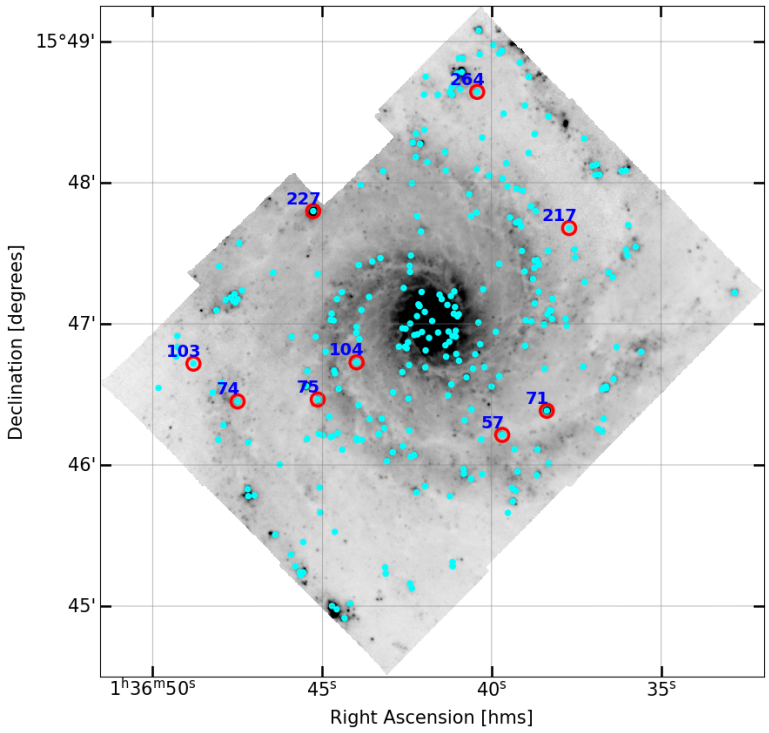

Figure 3.9: Isolated and bright point sources for the determination of the aperture correction to the photometry of PNe emission lines. The 9 point sources highlighted in red, while the 280 point sources found with PHOTUTILS DAOFIND algorithm on the 200 Å-wide image [5061-5261 Å] are shown in blue.

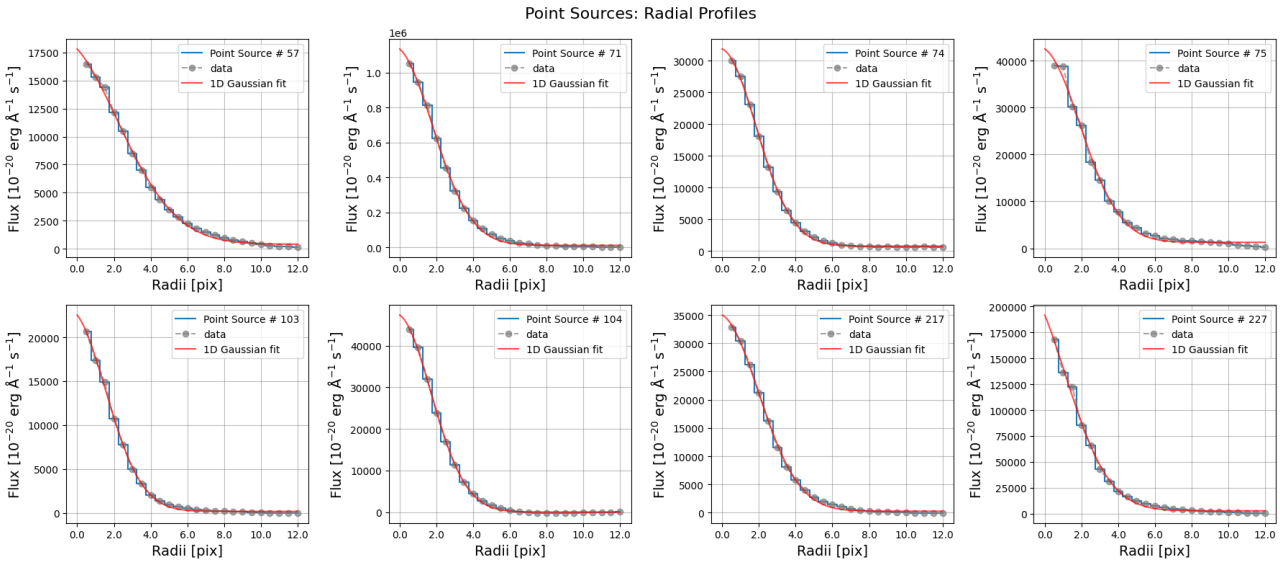

Figure 3.10: Radial profiles in [O III] for 8 of the 9 point sources from Figure 3.9. The median of the ratios of the fluxes within a very large radii over the flux within 3 pixels was taken as aperture correction in all six lines.

3.2.5 Step 5: Galactic Foreground Extinction

All measured fluxes underwent correction for Galactic foreground extinction. To account for the Milky Way foreground, we utilized the extinction curve developed by Cia89 with an R_V value of 3.1. The $E(B-V)$ values used were obtained from Schlafly and Finkbeiner (2011). Similar to Kre17, Rot21, and Sch22, we opted not to correct for internal extinction, whether it be due to circumstellar extinction associated with the PNe or dust present within the galaxy. The former was regarded as an essential component of the empirical calibration of the PNLF, with just a handful of studies addressing it (Davis et al., 2018). Regarding the latter, it was a common practice to refrain from applying corrections based on the research conducted by Feldmeier et al. (1997). Their findings suggest that for face-on galaxies, the anticipated extinction in $m_{[\mathrm{O\ III}]}$ is generally less than 0.1 magnitudes.

This notion is supported by Her08, who observed that the PNLFs for both the inner and outer disk of NGC 628 exhibit no significant differences. Since dust profiles generally exhibit exponential decrease, resulting in minimal extinction in the outer disk (Giovanelli et al., 1994; Muñoz-Mateos et al., 2009), the absence of radial variation in the PNLF suggests that central regions of NGC 628 also experience minimal extinction. If we assume that PNe are uniformly distributed in front of and behind the dust, we would anticipate observing roughly half of the sample with minimal extinction. As long as this subset accurately represents the bright end of the PNLF, we can obtain an accurate distance measurement.

3.2.6 Step 6: Conversion to Apparent Magnitudes

Lastly, the [O III] fluxes $F_{[\mathrm{O\ III}]}$ (in erg s^{-1} cm^{-2}) were transformed into apparent magnitudes employing the formula suggested by Jacoby (1989).

$$m_{[\mathrm{O\ III}]} = -2.5 \log F_{[\mathrm{O\ III}]} - 13.74 \tag{3.1}$$

3.3 Emission Line Diagnostics

Ensuring the authenticity of identified PNe candidates is vital in order to prevent contamination from SNR, compact H II regions, background galaxies, or even active galactic nuclei. Failing to distinguish these objects accurately can distort the PNLF's bright-end cutoff M^* and result in an underestimated galaxy distance. While it is relatively straightforward to identify cases of single emission-line interlopers lacking [O III] λ 4959 and/or Hα, the spectra of SNR and compact H II regions can resemble those of PNe. Furthermore, spatially overlapping PNe, which may appear as a single prominent entity in narrow-band images, can only be distinguished spectroscopically if their radial velocities exhibit a difference of approximately 100 km/s or more.

Within our 1009-long sample of [O III] emitters, we have not only identified PNe but also compact H II regions and recent SNR. To distinguish contaminants from our PNe candidate sample among all the [O III] detections, we have also measured line fluxes of Hβ, Hα, [N II] λ6584 Å, [S II] $\lambda\lambda$6717, 6737 Å with the same apertures. By combining the emission from these lines, we can utilize diagnostic ratios to determine the most probable ionizing source for each of the 1009 [O III] line emitting detections.

NGC 628 exhibits ongoing star formation, indicating that the observed [O III] emission is not solely attributed to PNe, but can also arise from SNR or compact H II regions. Hence, to differentiate and exclude these sources from our catalogue of PNe candidates, we employ a series of emission line diagnostics. Each object class (PNe, H II regions, and SNR) has a unique source of ionizing radiation, with PNe being associated with white dwarfs, H II regions with O and B stars, and SNR with shocks. As a result, their spectra exhibit different characteristics that can be employed to differentiate between them.

To distinguish PNe from H II regions and SNR, various complementary classification schemes have been implemented. Given their empirical nature, these schemes have evolved over time as better quality data has been gathered, while, on the other hand, the main scientific objectives were not always to filter out PNe specifically, but to classify instead other objects such as AGNs, H II regions, SNR, Seyferts, LINERs, etc. Hence, instead of applying a single criteria, we have adopted several classification schemes which are presented next.

3.3.1 Diagram I

Kewley et al. (2001) (Kew01) found that, within a realistic range of metallicities and ionization parameter range, continuous starburst models always fall below and to the left of an empirical limit on these diagrams [5]:

- $\frac{[\text{N II}]\lambda 6584}{\text{H}\alpha}$ _ $\frac{[\text{O III}]\lambda 5007}{\text{H}\beta}$
- $\frac{[\text{S II}]\lambda\lambda 6717{,}31}{\text{H}\alpha}$ _ $\frac{[\text{O III}]\lambda 5007}{\text{H}\beta}$
- $\frac{[\text{O I}]\lambda 6300}{\text{H}\alpha}$ _ $\frac{[\text{O III}]\lambda 5007}{\text{H}\beta}$

Figure 3.11 presents the first relation, where the classification boundary introduced by Kauffmann et al. (2003) (Kau03) is represented by the red dotted-dashed line. This boundary separates line ratios primarily influenced by star formation (left side of the line) from those dominated by AGN emission (right side of the line). It is crucial to acknowledge that this classification was established based on observations of nearby galaxies and may not be applicable to samples at high redshift. On the other hand, the blue solid line corresponds to the "maximum starburst" boundary line, which represents the theoretical limit proposed by Kew01[6].

Although both relations aim to indicate the upper limits of line ratios for emission lines primarily driven by star formation, the Kew01 curve is positioned higher than the Kau03 curve. This difference emerges due to the utilization of a stellar population synthesis model featuring a harder UV spectrum in the Kew01 curve, attributed to the particular treatment of Wolf-Rayet stars in the model [7] (Baugh et al., 2021). In Figure 3.11, the symbol sizes are scaled according to the apparent magnitudes of the [O III] λ5007 line. For the estimation of the PNLF, we utilize the Kau03 line[8], which is less restrictive and results in a larger sample of PNe. We will refer to this diagram as "DiagI."

[5] Given weak/irregular emission profiles in [O I] we have not computed the latter diagram.

[6] Only for illustrative purposes, we also show the shaded rectangular regions indicating H II regions, Seyferts, and LINERs, as obtained from Ho et al. (1997) criteria.

[7] For a thorough analysis and comparison of emission line properties using various population synthesis and photoionization models, please consult D'Agostino et al. (2019).

[8] Due to the ambiguity between PNe and H II regions, a version of our PNLF was also obtained with Kew01 boundary line, yielding almost identical (to within ± 0.01 mag) distance modulus results.

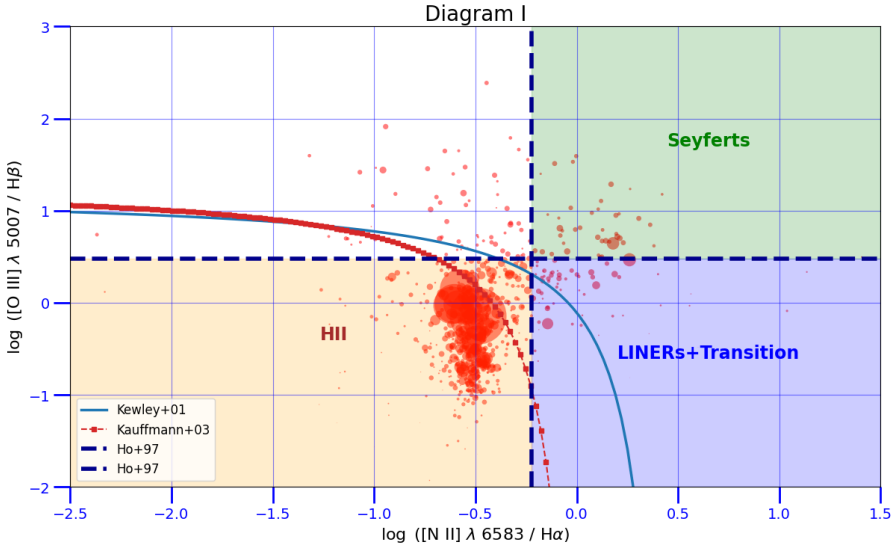

Figure 3.11: Diagram I: Kew01 extreme starburst classification line (blue solid line), and Kau03 pure star formation line (red dotted-dashed line). Marker sizes are proportional to $m_{[\mathrm{O\ III}]}$.

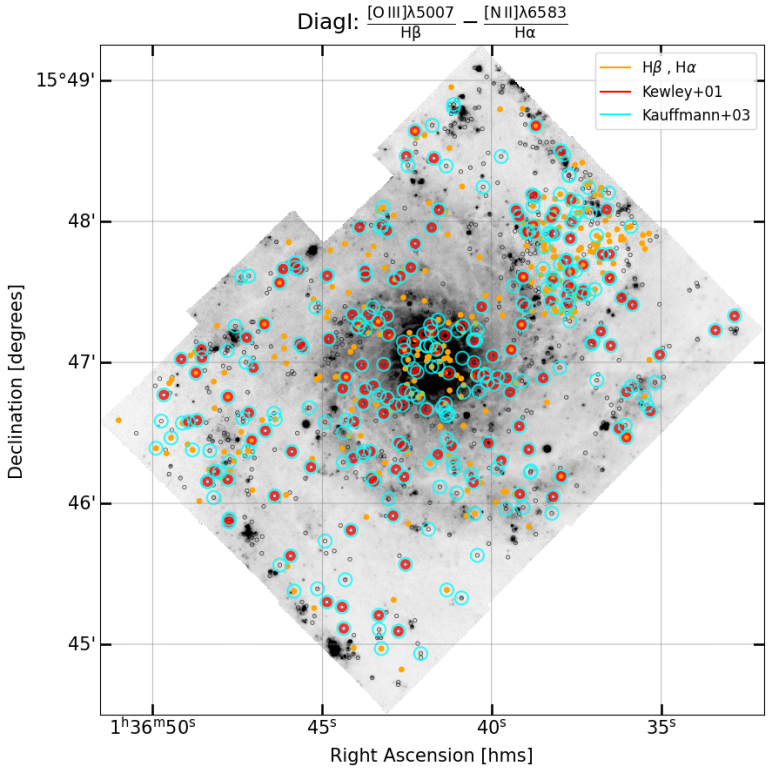

Figure 3.12: PNe above Kew01 (red) and Kau03 (cyan) lines, and with negative fluxes in either Hβ or Hα (orange).

3.3.2 Diagram II

We employed a similar approach to Rot21 by adopting the scheme introduced by Frew and Parker (2010) for the classification of emission line objects. This scheme utilizes the [O III]/Hβ line ratio plotted against the [S II]/Hα ratio, where [S II] represents the combined flux of the [S II] doublet $\lambda\lambda$ 6717, 6731 Å. This modified version of the original BPT diagram by Baldwin et al. (1981) offers advantages such as insensitivity to dust extinction and effective discrimination between different types of emission line objects, similar to DiagI.

Figure 3.13 showcases this diagram for the entire mosaic, illustrating the regions occupied by PNe, SNR and H II regions[9]. Rot21 note that, while the separation between PNe and SNR is well-defined based on empirical data from Sabin et al. (2013), the demarcation between PNe and H II regions, as defined by Kew01, is less distinct. Following the original work by Kew01, we identify sources as PNe if they lie to the right and above the Kew01 line. The figure also demonstrates that objects with significantly higher [O III] luminosities than the PNLF bright-end cutoff M^* are reliably positioned in the H II region area of the diagram. Conversely, the cluster of objects identified as PNe display [O III]/Hβ ratios above 5 (0.7 in log10 terms). We will refer to this diagram as "DiagII."

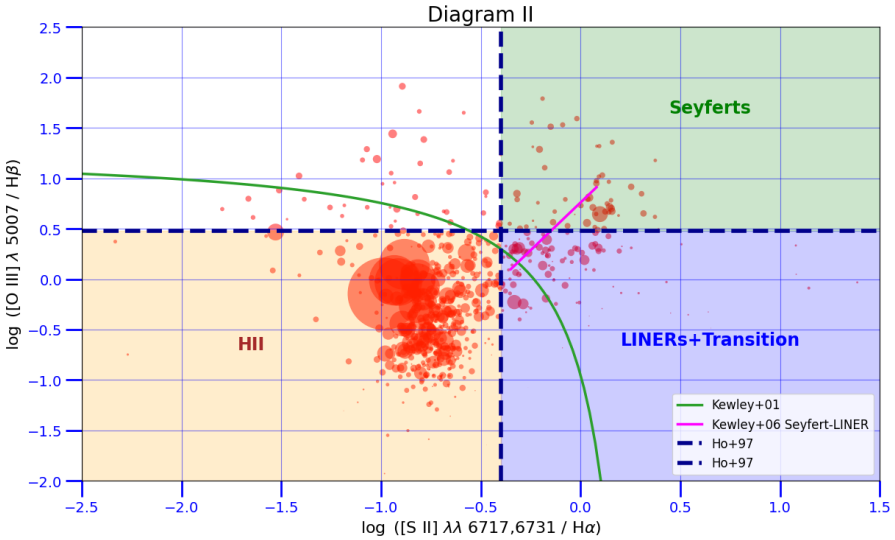

Figure 3.13: Diagram II: Kew01 extreme starburst classification line (green solid line) and Kew06 Seyfert–LINER line (magenta inclined solid line). Marker sizes are proportional to the $m_{[\mathrm{O\ III}]}$.

Both DiagI and DiagII diagrams have been used recently as classification tools in related literature. Casasola et al. (2018) did a spectroscopic characterization of the protocluster of galaxies around 7C 1756+6520, while Yao et al. (2020) developed a new diagnostic for separating SF regions from AGN in the GAMA G23 region, making use of WISE photometry. Baugh et al. (2021) used DiagI in the modelling of emission lines in star-forming galaxies at low, intermediate and high redshift. Soemitro et al. (2023) used DiagII to identify PNe to derive the distance to NGC 300 using the PNLF.

3.3.3 Diagrams III and IV

The classification schemes DiagI and DiagII were originally developed for the classification of galaxies and other extended [O III] emission-line objects such as H II regions or SNR. We decided to complement such schemes with additional tools in an attempt to validate our results, based on a successful removal of the main contaminants in our 1009-long PNe candidate sample, mostly SNR and H II regions.

As Sch22 note, it is important to highlight that the central star of a bright planetary nebula PNe exhibits considerably higher temperature compared to the star(s) responsible for ionizing an H II region. This leads to a steeper spectrum and an increased production of doubly-ionized oxygen in comparison to Hα (Shaver et al., 1983). As a result, the ratio of [O III] to (Hα + [N II]) is expected to exceed 1.6 (0.20 in log10 terms). Since narrowband imaging cannot separate the individual lines of Hα and [N II], they are typically treated as a combined measurement. This distinction becomes more significant for bright PNe, which often display even higher ratios. We apply the criterion established by

[9]Only for illustrative purposes, we present the Seyfert-LINER line (magenta inclined solid line) introduced by Kewley et al. (2006) (Kew06), which serves to distinguish galaxies into different categories including H II-region-like, Seyferts, LINERs, and composite H II-AGN types, as well as the rectangular regions obtained from Ho et al. (1997) criteria.

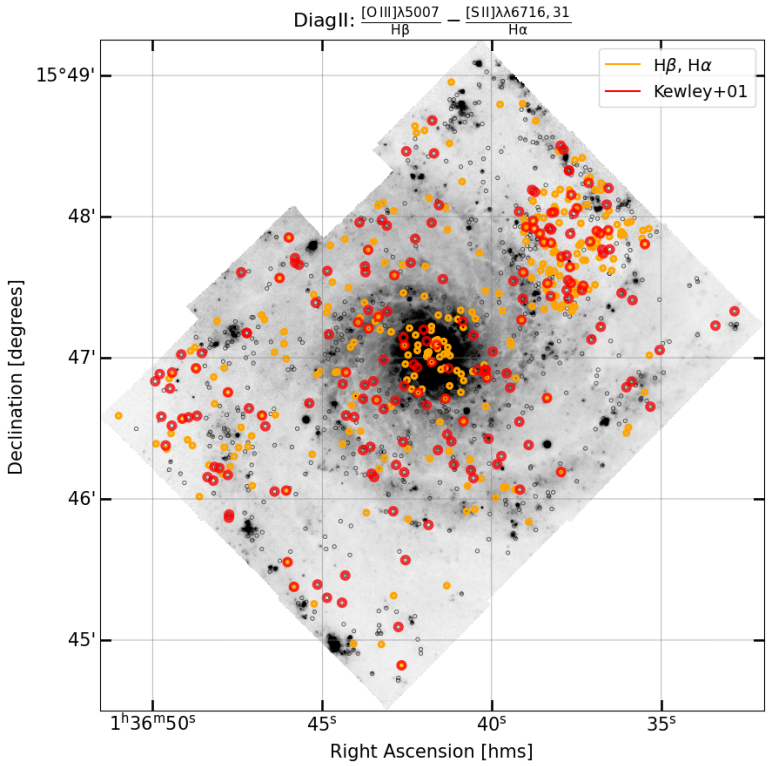

Figure 3.14: PNe candidates above Kew01 line (red), and with negative fluxes in either Hβ or Hα (orange).

Ciardullo et al. (2002) (Cia02), where PNe generally occupy positions above a boundary determined by,

$$4 > \log\left(\frac{F_{[\mathrm{O\ III}]\lambda5007}}{F_{\mathrm{H}\alpha} + F_{[\mathrm{N\ II}]\lambda6583}}\right) > -0.37M_{[\mathrm{O\ III}]} - 1.16, \tag{3.2}$$

with an upper limit of 4, determined empirically by considering the Hα + [N II] line to compensate for the presence of [N II] contamination within the narrowband filters, take into account the gas-phase metallicity of NGC 628. In this galaxy, H II regions tend to have a higher Hα flux compared to [O III] (Shaver et al., 1983), whereas PNe show the opposite trend (Baldwin et al., 1981)[10].

On the other hand, in order to address the potential contamination from compact SNR, the other major contaminant in our initial PNe candidate sample, we also checked the criterion established by Blair and Long (2004) (BL04). The material within SNR that has been heated by shocks exhibits higher [S II] to Hα ratios, specifically with,

$$\log\left(\frac{F_{[\mathrm{S\ II}]\lambda6717} + F_{[\mathrm{S\ II}]\lambda6731}}{F_{\mathrm{H}\alpha}}\right) > -0.4 \tag{3.3}$$

Although there is a possibility of excluding some H II regions with this criterion, it is highly unlikely to eliminate legitimate PNe. By combining the classification schemes of (i) PNe from Cia02 (Figure 3.15), and (ii) for SNR contaminants from BL04 (Figure 3.16), we have another tool to clean out our PNe candidate sample from contaminants. Identifying and removing compact SNR poses a greater challenge as compared to other contaminants. While older SNR can extend up to approximately 100 pc, allowing for their resolution with MUSE, younger remnants are smaller, around 20 pc in diameter, remaining unresolved at this spatial scale (Franchetti et al., 2012). Although none of the three known supernovae (SN 2002ap, SN 2003gc, SN 2013ej) in NGC 628 fall within our observed fields, previous studies examining diagnostic line ratios in populations of SNR, H II regions, and PNe

[10]A distance modulus of $m - M$ = 29.89 mag (in line with recent PNLF-based estimates (Kre17, Rot21, Sch22) was adopted to obtain the absolute [O III] magnitudes.

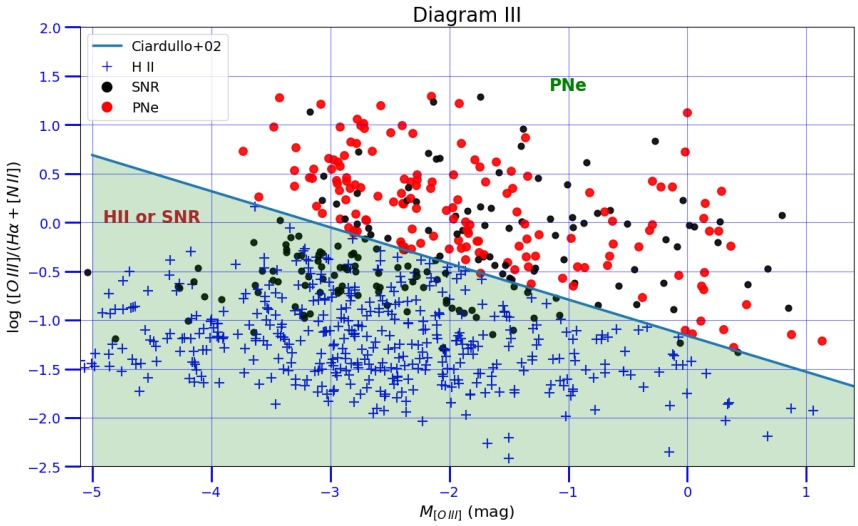

Figure 3.15: Diagram III: Ciardullo et al. (2002) classification scheme, based on Equation 3.2. Candidates above the line are deemed to be PNe, with potential SNR contaminants. A distance modulus of $m - M = 29.89$ mag, in line with both recent PNLF-based estimates (Rot21, Sch22) and values obtained in this study, was adopted to obtain the absolute [O III] magnitudes.

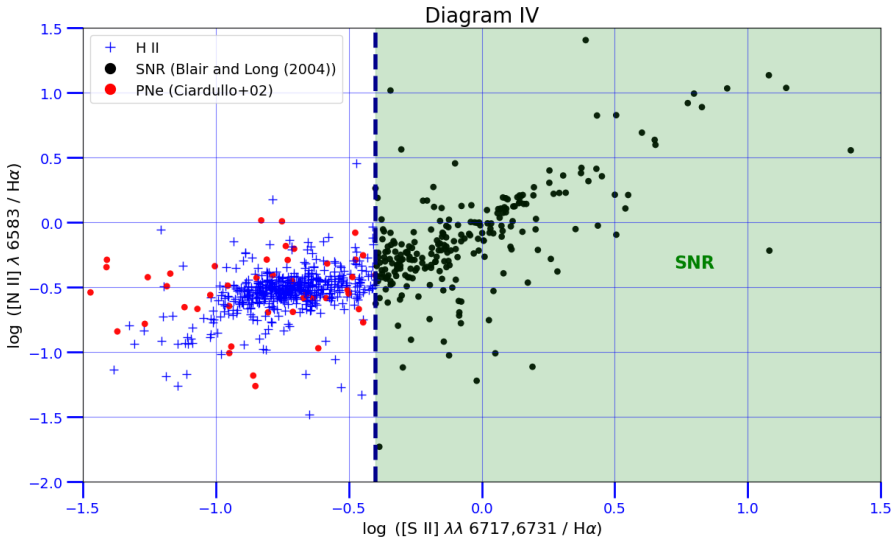

Figure 3.16: Diagram IV: Blair and Long (2004) classification scheme, based on Equation 3.3. Candidates to the right of the threshold value - 0.4 are deemed to be SNR.

(Sabbadin et al., 1977; Riesgo and López, 2006) indicate that these sources occupy distinct regions in a diagram comparing Hα/[N II] and Hα/[S II] line ratios. Although a significant number of our PNe candidates are not found in these regions, we can still employ the line ratios to detect contaminants within our sample, if any.

Figure 3.17 below shows the PNe identified with Cia02 (Equation 3.2) with and without the exclusion of the SNR from BL04 criteria (Equation 3.3): out of the 233 PNe above Cia02 line, after excluding the SNR, we only get 154 PNe. Ho et al. (1997) (Ho97) previously established an alternative classification scheme for different object classes based on the emission-line ratios of 418 galaxies. We overlay this classification scheme onto Diagrams I and II presented earlier by two green dashed horizontal/vertical lines, resulting in H II regions, Seyferts and LINERs.

Considering only the sources that satisfy $\frac{[\mathrm{S\ II}]\lambda\lambda 6713,31}{\mathrm{H}\alpha} < 0.4$ and $\frac{[\mathrm{N\ II}]\lambda 6583}{\mathrm{H}\alpha} < 0.6$ (i.e. H II nuclei regions as per Ho97 criteria), we show in Figure 3.18 such regions as well as the sources that were (residually) classified as H II regions after the previous identification of PNe and SNR from Cia02 and BL04, respectively, following Kre17 and Sch22. Interestingly, both classification approaches result

in almost the same number of H II regions ($\sim$ 580 from the 1009-long PNe candidate list).

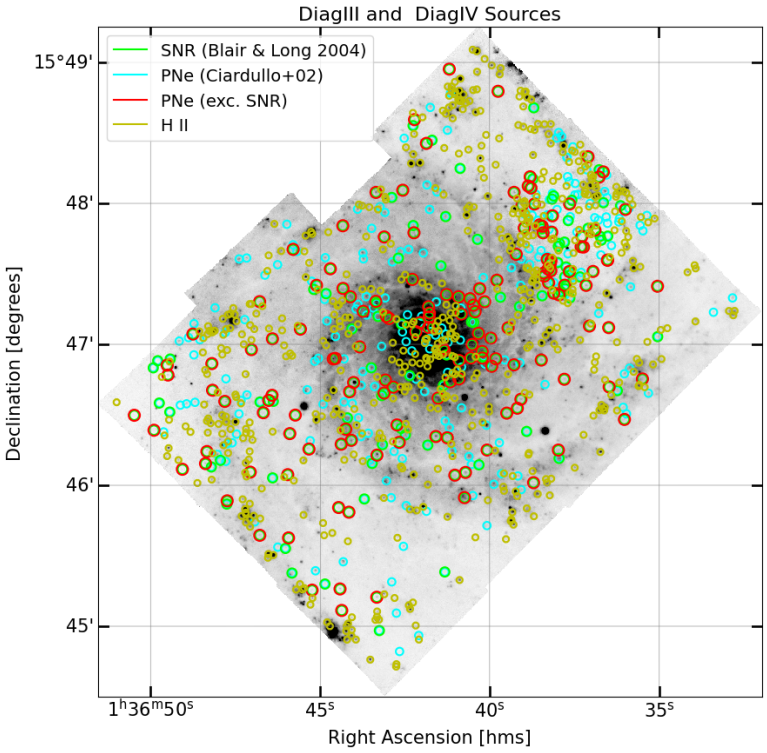

Figure 3.17: PNe identified with Ciardullo et al. (2002) criteria, with (red) and without (cyan) removal of SNR from Blair and Long (2004) criteria: 233 vs 154 planetaries.

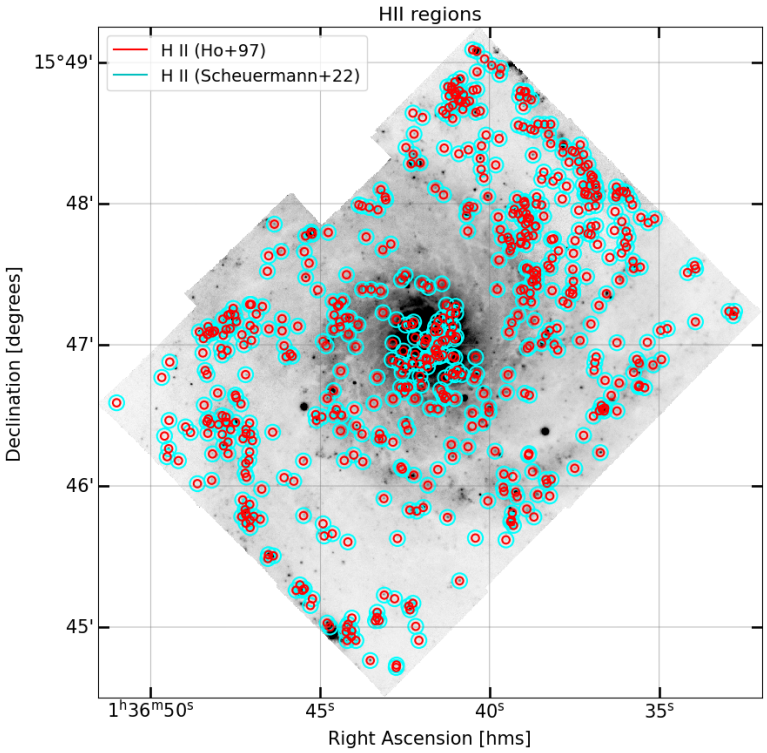

Figure 3.18: H II regions. (Ho et al., 1997): sources that satisfy $\frac{[\text{S II}]\lambda\lambda 6713,31}{\text{H}\alpha} < 0.4$ and/or $\frac{[\text{N II}]\lambda 6583}{\text{H}\alpha} < 0.6$. These sources match the H II regions residually obtained from Cia02 (Equation 3.2) and BL04 (Equation 3.3) criteria.

3.4 PNe Selections

The classification schemes described above are (i) empirical in nature, and (ii) not always targeted towards the identification of PNe. Hence, we have taken a conservative approach by using different schemes in order to filter out the contaminants (mostly H II regions and SNR) from our 1009-long PNe candidate sample. In particular, in order to have final PNe samples, based on the emission line ratios used so far, we have used the following individual criteria into various selection criteria:

- sources above Kew01 line in DiagI diagram (Figure 3.11)
- sources above Kau03 line in DiagI diagram (Figure 3.11)
- sources above Kew01 line in DiagII diagram (Figure 3.13)
- sources above Cia02 line after exclusion of SNR with BL04 criteria (Figures 3.15 and 3.16)
- sources identified as H II regions from Ho+97 criteria (Figure 3.18)
- sources with either negative flux in Hβ and/or Hα (Figures 3.11 or 3.13)

The last criteria was added to account for those sources with a negative net flux, after the continuum's subtraction, in the lines of Hβ and/or Hα. In a typical bright PNe, Hβ about 10 times fainter than [O III] (Herrmann et al., 2008), so obtaining accurate measurements is a challenge.

Table 3.3 shows the relevant counts for each of these criteria. Due to the uncertainty associated with the removal of contaminants from our PNe candidate sample, we estimate the distance modulus for the three PNe selections listed in Table 3.4, which result from different selection criteria (based on Diagrams I-II-III-IV). The last four columns show the total count of PNe, the number of overluminous sources (OL) excluded from the fit, and the number of PNe actually used in the fit in absolute (< 28.0 mag) and percentage (%) terms[11]. We performed a quick check on the three PNe selections to

Table 3.3: Selection criteria for the final PNe sample (D ≡ Diag).

Criteria	Reference	Lines	#	Object	Comments
DiagI-kw	Kew01	$\frac{[\mathrm{O\ III}]}{\mathrm{H}\beta}$ - $\frac{[\mathrm{N\ II}]}{\mathrm{H}\alpha}$	166	PNe	above Kew01 in DI
DiagI-kf	Kau03	$\frac{[\mathrm{O\ III}]}{\mathrm{H}\beta}$ - $\frac{[\mathrm{N\ II}]}{\mathrm{H}\alpha}$	294	PNe	above Kau03 in DI
DiagII-kw	Kew01	$\frac{[\mathrm{O\ III}]}{\mathrm{H}\beta}$ - $\frac{[\mathrm{S\ II}]}{\mathrm{H}\alpha}$	182	PNe	above Kew01 in DII
PNe-cia	Cia02	$\frac{[\mathrm{O\ III}]}{\mathrm{H}\alpha+[\mathrm{N\ II}]}$ - $M_{[\mathrm{O\ III}]}$	233	PNe, SNR	above Cia02 in DIII
SNR-bl	BL04	$\frac{[\mathrm{S\ II}]}{\mathrm{H}\alpha}$	272	SNR	right BL04 in DIV
PNe-sch	Sch22	$\frac{[\mathrm{O\ III}]}{\mathrm{H}\alpha+[\mathrm{N\ II}]}$ - $M_{[\mathrm{O\ III}]}$, $\frac{[\mathrm{S\ II}]}{\mathrm{H}\alpha}$	154	PNe	above Cia02 (DIII) + left BL04 (DIV)
HII-ho	Ho97	$\frac{[\mathrm{N\ II}]}{\mathrm{H}\alpha}$, $\frac{[\mathrm{S\ II}]}{\mathrm{H}\alpha}$	583	HII	left Ho+97 (DI and DII)
PNe-HβHα	-	Hβ - Hα	290	PNe	$I_{\mathrm{H}\beta} < 0$ and/or $I_{\mathrm{H}\alpha} < 0$

Table 3.4: PNe sample selections.

PNe Sample	DiagI-kw	DiagI-kf	DiagII-kw	PNe-sch	PNe-HβHα	Count (#)	OL (#)	(< 28.0 mag) (#)	%
PNe1	✖	✔	✖	✖	✔	514	0	279	45.7
PNe2	✖	✖	✔	✖	✔	426	1	198	53.4
PNe3	✖	✖	✖	✔	✔	392	0	166	57.5

[11] We calculated the distance modulus by combining the individual criteria in Table 3.1 resulting in 20 different PNe selections. In almost all cases, results were consistent with the distances presented in this work for the three PNe selections under consideration.

eliminate any non-point-like objects that may have been included during the previous selection process, based on the FWHM estimated from the 1D Gaussian fits and the sharpness estimates obtained from DAOPHOT. Additionally, we also checked for those objects with an unusually high luminosity compared to the remaining luminosity function, indicating that they cannot be described by the PNLF. These OL objects have been observed in some previous PNe studies but their exact origin remains uncertain. Possible explanations include the chance occurrence of two PNe in close proximity, misclassified H II regions, or background Ly-α galaxies.

When an object is located close to the brighter end of the PNLF, it becomes difficult to remove it from the sample, which can result in underestimating distances. However, if there is a noticeable gap compared to the rest of the sample, it becomes easier to exclude such objects based on the poor fit quality they would exhibit. As per column OL in Table 3.4, we only excluded the most excessively luminous source from the PNe2 selection.

Chapter 4

Results

4.1 Fitting the Luminosity Function

The PNLF is an empirical relationship that predicts the number of observed PNe based on their luminosity. Cia89 developed a methodology that combines an exponential function from theoretical evolutionary models with a cutoff M^* at the bright end of the PNLF. The PNLF is described by the analytical form,

$$N(\mathrm{M_{[O\ III]}}) \propto e^{0.307\mathrm{M_{[O\ III]}}} \left(1 - e^{3(\mathrm{M^*} - \mathrm{M_{[O\ III]}})}\right) \tag{4.1}$$

In spite of alternative parametrizations being proposed, this simplified form of the luminosity function has remained widely accepted. For example, Hartke et al. (2017) considered the slope of the faint end (originally 0.307) as a free parameter, while it has also been used a fully numerical luminosity function (Méndez et al., 2001; Teodorescu et al., 2011).

The zero-point M^*, which is determined by the luminosity of the brightest PNe, plays a crucial role in distance determination rather than the functional form itself. To determine this value, PNe in galaxies with known distances are used. The initial value of $M^* = -4.48$ mag was originally derived by Cia89 based on the Cepheid distance measurement to M31. In a subsequent study, Cia02 investigated 27 galaxies with distances obtained from the Hubble Space Telescope Key Project to assess the influence of metallicity on the zero-point. They found a moderate dependence, with an increase observed at lower metallicities. In the case of NGC 628, given that the metallicity is measured to be 12 + log(O/H) = 8.50 (Kreckel et al., 2019; Scheuermann et al., 2022), it is unlikely to be affected by it.

Therefore, the zero-point M^* is the most crucial factor in determining the PNLF. In our analysis, we adopt a value of M^* = -4.47 mag as in Kre17 and Sch22. Recent research has used the following PNLF cutoff M^* values for NGC 628:

- **Kre17:** M^* = $-4.47^{+0.02}_{-0.03}$ mag[1], noting that this value is applicable for galaxies with solar metallicity like NGC 628 (Cia02). Updated calibrations propose a slightly higher value $M^* = -4.53 \pm 0.06$ (Ciardullo, 2012); nonetheless, this would only result in a $\sim$3% adjustment to our distance estimation and remains consistent within the margins of error.

- **Rot21:** M^*=-4.53, which is the most probable value derived by Ciardullo (2012) from a collection of approximately twelve neighbouring galaxies with accurately determined Cepheid and TRGB distances.

The resulting curve was fitted to the three PNe selections with Python-based Scipy statistical library[2]. For the fitting of the PNLF (Equation 4.1) to the three PNe selections described in Table 3.4,

[1] Same value was used in Her08.

[2] It is worth mentioning that it is customary to perform the fitting process by convolving the empirical PNLF with

we considered four different binnings spanning the magnitude interval from 25.0 mag to 28.0 mag (the cutoff), namely: $n_{\rm bins}$ = [8, 10, 14, 18]. Table 4.1 shows the number of data points used for the fitting and the associated magnitude intervals of the four different binnings.

Table 4.1: PNLF fitting.

$n_{\rm bins}$	8	10	14	18
Data Points (#)	7	9	13	17
$\Delta m_{[\rm O\ III]}$ (mag)	0.43	0.33	0.23	0.18

For the $n_{\rm bins} = [8, 10, 14, 18]$ binnings and for the three PNe selections described in Table 3.4 we show in Figure 4.1 the PNLF fits, with the error bars associated to each data point in the histograms (Poisson statistics). Figure 4.1 illustrates the bright end of the PNLF for the four binnings and the three PNe selections. Although our observations of PNe extend up to $m_{[\rm O\ III]} \sim 30.0$ mag, we limit our fit to the top $\sim$2.5 magnitudes of the PNLF's zero-point M^* at $m_{[\rm O\ III]} \sim 28.0$. This choice is influenced by the non-monotonic nature of the PNLF in star-forming populations, which deviates deviates from exponential growth as in Equation 4.1 at faint magnitudes and instead displays a distinct dip, typically ranging from two to four magnitudes below M^*, as observed by Jacoby and Marco (2002) and discussed in Ciardullo (2010). This choice contrasts to the 27.0, 26.9, and 28.0 cutoffs used in Kre17, Rot21 and Sch22, respectively. For the percentage of faint PNe excluded see Table 3.4 (last column).

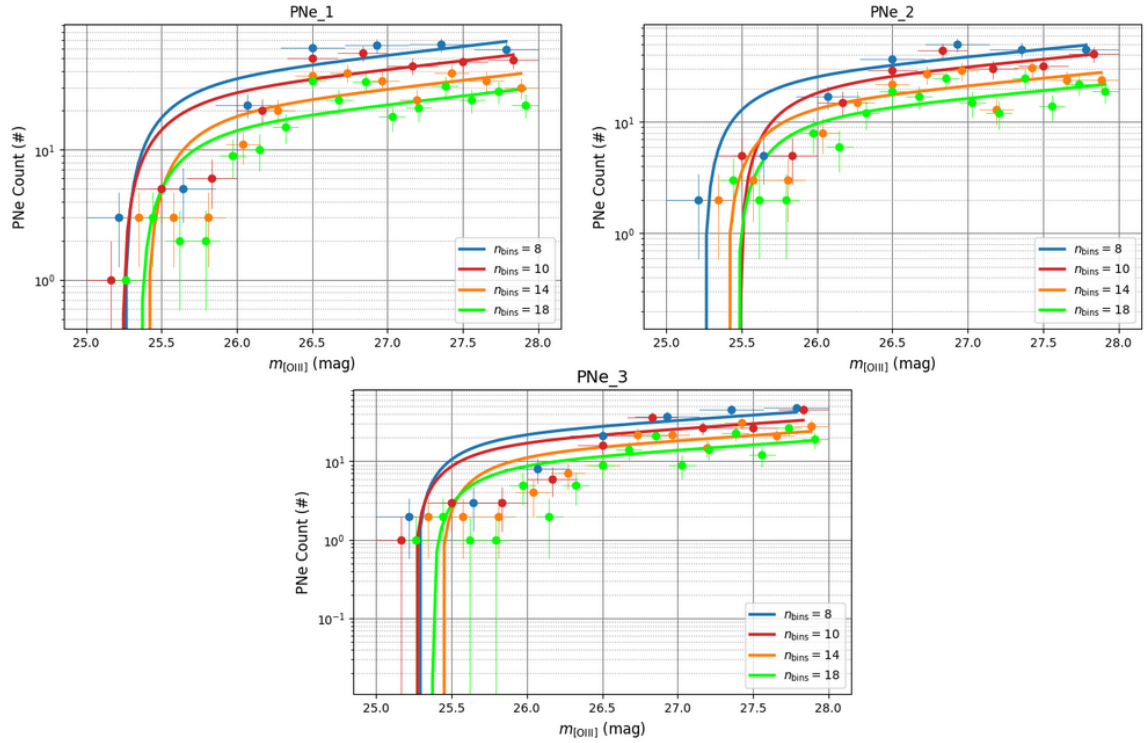

Figure 4.1: PNLF fits for the three PNe selections as shown in Table 3.4. A magnitude cutoff of 28.0 mag was applied. The y-errors in the fits were determined based on Poisson statistics, while the x-errors represent the bin widths.

estimated photometric errors. Subsequently, the PNe brighter than a specific completeness limit are fitted to the convolved function using the maximum likelihood method (Ciardullo et al., 1989).

4.2 Distance modulus

Taking into consideration the potential impact of foreground galactic extinction we assumed $E(B-V) = 0.062$ (Schlafly and Finkbeiner, 2011), $R_V = 3.1$ and Cia89's extinction law ($A_V \sim 0.2$), our distance modulus estimates are presented in Table 4.2. The uncertainties presented here solely account for the statistical errors associated with the fit. These values show great consistency among the three PNe selections and the four binnings. It is also worth noting that the brightest PNe in Rot21 sample also appears as the most OL (excluded) source in our PNe2 selection, which is consistent as it uses the same classification scheme (DiagII). In the sample studied by Rot21, this particular PNe stands out as being 0.11 magnitudes brighter than the next brightest source. Although it does not strictly fall into the category of an overluminous object, they have included it in their PNLF fitting analysis. Nonetheless, by excluding this object they also found a best-fit solution that was approximately 90 times more likely, leading to a larger distance from $29.76^{+0.03}_{-0.05}$ to $29.87^{0.05}_{-0.03}$, which is more in line with our results with PNe2 selection.

Table 4.2 shows the estimates for the distance modulus and associated fitting errors for the four binnings considered and the three PNe selections. Figure 4.2 shows the distance modulus $m - M$ estimates with the corresponding error bars from the optimization fitting algorithm.

Table 4.2: Distance modulus $m - M$ and Distances D estimates.

PNe Selection	$m - M$ (mag)			
	$n = 8$	$n = 10$	$n = 14$	$n = 18$
PNe1	29.74 ± 0.08	29.99 ± 0.07	29.89 ± 0.05	29.85 ± 0.05
PNe2	29.74 ± 0.07	29.98 ± 0.07	29.88 ± 0.06	29.97 ± 0.06
PNe3	29.75 ± 0.08	30.01 ± 0.08	29.91 ± 0.07	29.83 ± 0.06

PNe Selection	D (Mpc)			
	$n = 8$	$n = 10$	$n = 14$	$n = 18$
PNe1	8.80 ± 0.29	8.74 ± 0.27	9.43 ± 0.26	9.23 ± 0.24
PNe2	8.80 ± 0.26	9.80 ± 0.30	9.41 ± 0.27	9.70 ± 0.27
PNe3	8.86 ± 0.32	8.79 ± 0.34	9.53 ± 0.29	9.30 ± 0.28

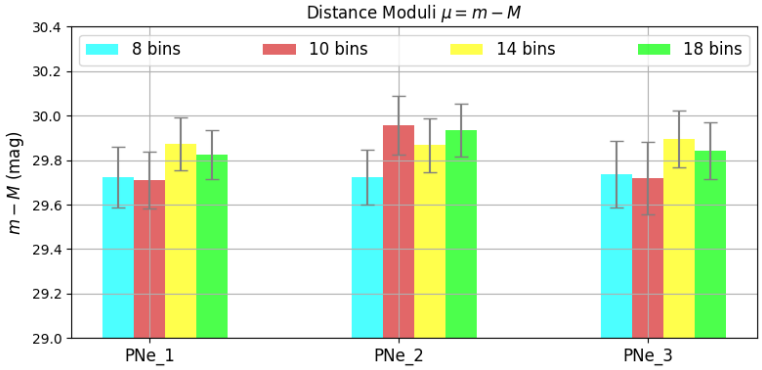

Figure 4.2: Distance modulus $\mu = m - M$ from the PNLF fits for the three PNe selections (see Table 3.4).

Chapter 5

Discussion

5.1 Comparison with literature distances

As shown in Table 5.1 NGC 628 is estimated to be located at a distance of 7.3 to 10.2 Mpc based on measurements of the TRGB, from 6.7 to 10.0 Mpc based on SN II standard candles, and from 7.2 to 9.6 Mpc using the brightest supergiants, among various techniques. Four PNLF distances also exist in the literature, namely: Her08's photometry, based on interference filters, suggests a distance of 8.6 Mpc, whereas Kre17's analysis found a 9.6 Mpc estimate, noting that their larger distance compared to Her08's one is due to the capability of MUSE to exclude SNR from the sample of PNe. More recent PNLF-based distance estimates are those from Rot21 (8.9 Mpc) and Sch22 (9.5 Mpc). Davis et al. (2018) argue that SNR rarely affect PNLF distance estimates, something that Sch22 and this study indeed finds, in contrast to Kre17. It is worth noting that Kre17 and Sch22 note that SNR are the most difficult contaminant to identify and remove from PNe samples, while Rot21 finds harder to differentiate H II regions.

In Figure 5.1 we compare our representative estimate with PNe2 and 14 bins and different PNLF-based distance modulus for NGC 628 in the existing literature. As it can be seen, our results are in excellent agreement with the PNLF-based distances.

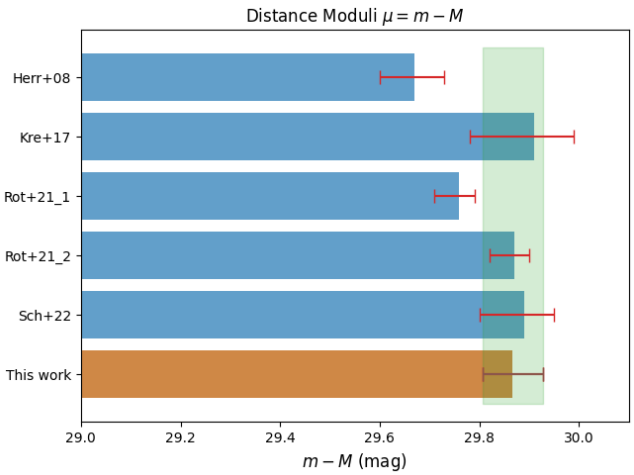

Figure 5.1: Comparison of PNLF-based distance measurements for NGC 628 with values reported in the literature. The representative value obtained in this study with PNe2 selection (based on DiagII) and 14 bins is marked by a brown bar with the error bands shaded in green ($m - M = 29.88 \pm 0.06$ mag (9.41 ± 0.25 Mpc).

Table 5.1: Comparison of Distance modulus for NGC 628.

$(m-M)$ (mag)	D Mpc	Method	Reference
31.46		H II Regions	Bottinelli et al. (1984, 1985)
26.62 ± 0.62		Tully-Fisher Relation	Bottinelli et al. (1984, 1985)
29.93 ± 0.43	9.70	Tully-Fisher Relation	Tully (1988)
29.87	9.40	Gravitational Stability Gas Disc	Zasov and Bizyaev (1996)
29.30	7.24	Brightest Supergiants	Sohn and Davidge (1996)
29.32 ± 0.40	7.31 ± 1.35	Brightest Supergiants	Sharina et al. (1996)
29.13	6.70	SN II Standard Candle	Vinkó, J. et al. (2004)
29.91 ± 0.63	9.59 ± 2.78	SN II Standard Candle	Hendry et al. (2005)
29.91 ± 0.49	9.59 ± 2.16	Brightest Supergiants	Hendry et al. (2005)
29.44 ± 0.48	7.73 ± 1.71	Brightest supergiants	Hendry et al. (2005)
29.29	7.20	SN II Standard Candle	Van Dyk et al. (2006)
29.91 ± 0.40	9.59 ± 2.78	SN II Standard Candle	Hendry et al. (2005)
$29.67^{+0.06}_{-0.07}$	$8.59^{+0.24}_{-0.28}$	PNLF (narrow-band)	Herrmann et al. (2008)
29.32 ± 0.40	7.31 ± 1.35	TRGB	Jacobs et al. (2009)
29.99 ± 0.42	9.95	SN II Standard Candle	Olivares et al. (2010)
29.98 ± 0.55	9.91	SN II Standard Candle	Olivares et al. (2010)
29.98 ± 0.28	9.91	SN II Standard Candle	Olivares et al. (2010)
29.94 ± 0.54	9.73	SN II Standard Candle	Olivares et al. (2010)
30.04 ± 0.03	10.19 ± 0.14	TRGB	Jang and Lee (2014)
30.02 ± 0.03	10.09 ± 0.14	TRGB	Jang and Lee (2014)
29.76 ± 0.24	8.87 ± 0.99	SN II photospheric magnitude	Rodríguez et al. (2014)
29.74 ± 0.18	10.05 ± 0.74	SN II photospheric magnitude	Rodríguez et al. (2014)
30.01 ± 0.07	9.46 ± 0.32	SN II photospheric magnitude	Rodríguez et al. (2014)
29.88 ± 0.05	10.20 ± 0.22	SN II photospheric magnitude	Rodríguez et al. (2014)
$29.91^{+0.08}_{-0.13}$	$9.59^{+0.35}_{-0.57}$	PNLF	Kreckel et al. (2017)
29.95 ± 0.10	9.77 ± 0.49	TRGB	McQuinn et al. (2017)
$29.76^{+0.03}_{-0.05}$	8.95	PNLF (IFS)	Roth et al. (2021)
$29.87^{+0.03}_{-0.05}$	9.40	PNLF (with OL source)	Roth et al. (2021)
$29.89^{+0.06}_{-0.09}$	$9.52^{+0.26}_{-0.41}$	PNLF (IFS)	Scheuermann et al. (2022)
$29.90^{+0.06}_{-0.09}$	$9.55^{+0.26}_{-0.41}$	PNLF (IFS, inc. SNR)	Scheuermann et al. (2022)
29.88 ± 0.06	9.41 ± 0.27	PNLF (IFS)	This work

5.2 Binnings, Cutoff Point and the PNLF

In all three PNe selections the larger distance is obtained with the smaller number of bins (8), while the shorter distances are achieved by the larger 14 (PNe1 and PNe3 selections) and 18 (PNe2 selection) binnings. This is expected given the need to accommodate the brightest magnitudes toward the left-most bins in the coarser 8 binning.

In other words, what is crucial to note is the effect of the number of bins on the location of the first point of the PNLF. It is worth noting when interpreting the PNLF-based distances in the literature that Her08, Kre17, Rot21 and Sch22 used, approximately 0.35, 0.50, 0.25 and 0.35 Å -wide binnings, respectively, after visual inspection of their PNLF fits. Our binnings with 10 and 14 bins correspond to 0.33 and 0.23 Å widths. We have shown that the PNLF fit is primarily driven by the most luminous PNe, which influences the location of the cutoff point M^*, which, in turn, depends on the width of the bins. In this regard, and in relation to the number of bins when building a PNLF, it is important to ensure enough PNe in order to populate the brightest bins. On the other hand, because of the exponential distribution of the PNLF, the fainter PNe tend to shift the function towards larger distances. Therefore, if we only observe the brighter end, it is common to underestimate the distance.

All these effects are influenced by the binning used in the PNLF.

On the other hand, we have utilized a fixed value of $M^* = 4.47$ in our study. However, both theoretical models (Dopita et al., 1992) and observational findings (Cia02) suggest that M^* increases at lower metallicities. This variation can be approximated by a quadratic equation of the form (Sch22),

$$\Delta M^* = 0.928\,[\mathrm{O/H}]^2 - 0.019\,[\mathrm{O/H}] + 0.004, \tag{5.1}$$

with the solar oxygen abundance 12 + log (O/H) = 8.69 from Asplund et al. (2009). However, Ciardullo (2010) found that in galaxies with metallicities higher than that of the LMC, the zero-point remains relatively constant. Hence, given that NGC 628 is not a low metallicity galaxy, it seems safe to have considered such M^* value.

5.3 Contamination with SNR

Kre17 revealed that misclassified SNR can affect distance measurements obtained from the PNLF. This raised concerns about the adequacy of narrowband observations for PNe studies. SNR need to meet specific criteria to bias the results (Sch22): (i) being classified as PNe by narrowband studies, (ii) occurring at the bright end of the PNLF, and (iii) not being significantly brighter than M^*. Either just one SNR near the bright end or multiple fainter SNR are required to alter the distance. For our PNe3 selection, we re-estimated the distance modulus by only imposing the Cia02 criteria, i.e. the sources above the line in Figure 3.15, without removing the SNR right of BL04 boundary (Figure 3.16). For the four different binnings, the distance modulus increased by less than 0.04 mag. These findings are in line with those from Sch22 and support Davis et al. (2018)'s hypothesis of a relatively modest effect of SNR contaminants on PNLF-based distance estimations.

5.4 Error Sources

Rot21 elaborates on two significant factors contributing to the overall error budget, namely: (i) the calibration of the photometric zero-point, specifically the uncertainties associated with aperture correction and flux calibration, and (ii) the incomplete understanding of foreground extinction. The latter is a common challenge in many distance indicators and has improved over time with advancements in measuring the long-wavelength emission of dust (Aniano et al., 2020). As Rot22 note, future investigations may explore the potential of utilizing the MUSE data cube for independently estimating $E(B-V)$ through a stellar population analysis of the host galaxy (Zahid et al., 2017; Li et al., 2020, 2021).

Conversely, the former issue can be more problematic, particularly for a complex, narrow-field instrument like MUSE. The quality of the images (seeing) plays a crucial role in accurately determining PNLF. Improved image quality (say $0.''6$ compared to $1.''0$ seeing), greatly enhances the reach of PNLF and facilitates PNe identification in high surface brightness areas of galaxies. Rot21 mentions the MXDF project, which has demonstrated that using GLAO (Ground Layer Adaptive Optics) at UT4 of the VLT consistently achieves image quality of $0.''6$ at a wavelength of 5000 Å, making it highly beneficial for future PNLF observations.

Rot21 also stresses the fact that MUSE archival data contains numerous observations that have not been specifically optimized for accurate spectrophotometry suggesting that, in order to mitigate potential uncertainties arising from alterations in atmospheric transmission, supplementary flux calibrations both prior to and subsequent to PNLF exposures, ensuring that the airmass is comparable, should be conducted.

Finally, an additional crucial factor to consider highlighted by Rot21 relates to the determination of the aperture correction of a frame to ensure precise alignment of relative photometric measurements

on an absolute magnitude scale. Selecting fields that encompass adequately bright point sources assists in securing suitable PSF standards within each frame. Opting for higher angular resolution facilitates the identification of point sources. Once designated, the PSF stars can undergo analysis using MUSE.

5.5 Limitations of IFU observations for the PNLF

The practical application of the PNLF is generally limited to galaxies within a distance of 20 Mpc. Beyond this distance, the expected flux from a single PNe becomes comparable to the background noise, making it difficult to detect using narrowband imaging. However, recent studies by Ventimiglia et al. (2011), Rot21 and Sch22 have pushed the boundaries by employing multi-slit imaging spectroscopy or IFU spectroscopy techniques. Kre17 and Sch22 provide a rough estimation of the maximum measurable distance achievable using MUSE with comparable exposure times as those used in the observations of NGC 628 (42-49 minutes): both require a minimum number of $\gtrsim$ 20 PNe detections for reliable distance measurements.

According to Sch22, a decrease in resolution can result in a reduction in the number of detections, as fainter objects may blend into the background at coarser resolutions. However, Kre17 demonstrated that this concern only arises at physical resolutions exceeding 100 pc. Considering the typical seeing achieved with MUSE (0.″60 with adaptive optics and 0.″76 without), this corresponds to distances of 34.4 Mpc and 27.1 Mpc, respectively - both beyond the distance range of NGC 628. As a result, this issue primarily impacts less advanced IFU instruments with coarser spatial resolutions.

Studying PNe within galaxy disks offers significant advantages due to their correlation with stellar density. While narrowband imaging in these regions is challenging due to high background noise, employing full spectroscopic information allows for the detection of numerous PNe with limited spatial coverage. According to Kre17, for galaxies located at approximately twice the distance of NGC 628 (i.e., around 20 Mpc), the PNLF cutoff would be fainter by 1.5 magnitudes. To accurately trace the PNLF cutoff, a PNe survey depth of 0.8 magnitudes would be necessary. However, even with a small sample size of 20 PNe, it is possible to achieve accurate distance recovery within 3% with only a modest increase in uncertainty of approximately 10%. Based on Kre17's observations of PNe density in their three pointings (K1, K2 and P1), this would correspond to a survey area of approximately 15 kpc^2 within the central galaxy disc.

5.6 Overluminous Sources and Calibration of the PNLF

The MUSE instrument provides valuable information for understanding the nature of overluminous sources, helping to distinguish between PNe and contaminants. The reliability of PNLF-based distances hinges on two crucial questions: the precise shape of the PNLF's bright end and its potential variation with stellar population. Currently, these questions lack theoretical explanations.

Cia89 introduced the concept of truncating the power-law distribution of PNe based on the magnitude distribution observed in M31's bulge. This approach has generally proven reliable, but occasional identification of "overluminous" [O III] sources in PNe surveys poses challenges. Determining the true nature of these sources is difficult due to limited availability of spectroscopic follow-up. They could potentially be PNe, SNR, compact H II regions, blends of multiple objects, or even background galaxies. Addressing cosmological inquiries would require an adaptation of the empirical form of the PNLF if these objects are indeed genuine PNe within the target galaxy.

On the other hand, unlike methods like Cepheids or the TRGB, calibrating the PNLF within our Milky Way galaxy currently lacks immediate prospects. As a result, the PNLF serves as a *secondary* standard candle, and the distances derived from it inherently contain some degree of error originating from distance measurements to nearby galaxies. At present, the uncertainty associated with M^* is

approximately $\sim$0.04 mag (Ciardullo, 2013; Roth et al., 2021; Ciardullo, 2022), although MUSE observations of additional Cepheid and TRGB galaxies could improve this estimate.

5.7 Future Application for the PNLF Using MUSE

We have seen that the accuracy of distance estimations using the PNLF is significantly impacted by image quality (seeing). Simulation studies by Rot21 indicate notable differences in PNLF reach and the ability to identify PNe in high surface brightness regions when comparing image qualities of $1.''0$ and $0.''6$. Rot21 list some observing techniques aimed at improving the accuracy of PNLF-based distance estimations with MUSE. First, recent observations conducted as part of the MXDF project have showcased consistent achievement of an image quality of $0.''6$ using the GLAO system at UT4 of the VLT. Future PNLF investigations can greatly benefit from incorporating GLAO technology.

Second, choosing fields with relatively low surface brightness can also enhance PNLF measurements. Although high surface brightness regions tend to harbour more PNe, the primary source of noise in PNLF observations arises from the brightness of the underlying galaxy background and night sky. Hence, it is of the utmost importance to optimize the placement of MUSE pointings to achieve a maximum number of expected PNe while minimizing the number of fields needed to obtain a statistically meaningful PNe sample. The general objective is to encompass a minimum of 50 PNe within the $\sim$1 magnitude range where they appear brightest in the PNLF.

Moreover, thoroughly selecting galaxies is equally crucial to address various concerns. Investigating biases in PNLF distances beyond approximately 15 Mpc necessitates further exploration, which includes examining potential limitations in data quality, potential misclassification of other emission-line objects as PNe, and intrinsic errors within the PNLF itself (Roth et al., 2021; Ciardullo, 2022). Conducting MUSE observations on galaxies previously analysed in PNLF studies can assist in identifying and resolving some of these biases. Moreover, to extend PNLF distances to approximately 50 Mpc, it is crucial to focus on well-structured early-type systems as target galaxies. This approach minimizes confusion with H II regions and SNR while providing a sample of Type Ia supernovae for calibration. These galaxies, which are beyond the TRGB range and do not have Cepheid variables, would make a significant contribution to the calibration of Type Ia supernovae. Lastly, the development of BlueMUSE, featuring a larger field of view, higher throughput, and improved resolving power, holds significant promise for maximizing the potential of the PNLF.

Chapter 6

Summary and Conclusions

In this study, we have utilized spatially resolved spectrophotometry to validate previous PNLF-based distance estimates to the late-type spiral galaxy NGC 628. We utilized the MUSE instrument, an optical IFU on the VLT to conduct a comprehensive mapping of emission lines including Hβ, [O III], Hα, [N II], and [S II] within the central disk of NGC 628, covering an approximate area of 25 kpc^2. Our analysis involved the selection of unresolved [O III] emission line sources, enabling us to identify and differentiate contaminants within our sample. Using well-established criteria, we identified 514, 426 and 392 PNe sources within the twelve observation fields by the three selection criteria considered in this study (refer to Table 3.4).

By analysing the 279, 198 and 166 PNe with $m_{[\mathrm{O\ III}]} < 28.0$ mag, we determined a new PNLF distance modulus of -29.88 $\pm$0.06 mag (9.41 $\pm$ 0.27 Mpc) with selection PNe2 and 14 bins. This measurement is in good agreement (as well as those with PNe1 and PNe3 selections, and the rest of binnings) with existing literature values, particularly those studies also using the PNLF technique. This finding highlights the power of leveraging full spectral information provided by IFU observations compared to narrowband imaging when isolating the sample of PNe, while shedding light on the consistency among the different selection criteria used in the literature.

The key contributions of this paper are as follows:

1. We have implemented the DELF technique to enhance the accuracy of $m_{[\mathrm{O\ III}]}$ photometry, as described in Rot21.

2. We have evaluated the effectiveness of the DELF technique using archival data from the well-studied NGC 628.

3. Through the simultaneous measurement of [O III], Hβ, Hα, [N II], and [S II] using MUSE, a successful differentiation of PNe from various types of emission-line objects, including H II regions, SNR and background galaxies, has been achieved.

4. In contrast to existing literature, we have employed/combined different classification criteria to identify PNe sources from other [O III] emitting sources.

5. Based on these combined criteria, we have constructed different clean samples of PNe (the PNe selections), which has significantly contributed to a more precise determination of the bright end of the PNLF, which is susceptible to contamination by interlopers.

6. We have obtained similar distance estimates, within error limits, to NGC 628 as the existing four studies that also use the PNLF technique.

7. We have shown the effect on the distance modulus estimation of the number of binnings when fitting the PNLF.

Our findings affirm the continued reliability of the PNLF as a valuable standard candle. The distances obtained for NGC 628 in this study exhibit excellent alignment with earlier measurements, in particular those based on the PNLF technique. Since the PNe population correlates with stellar density, conducting PNe studies within galaxy disks offers distinct advantages. Previous efforts using narrowband imaging faced challenges arising from the intense (unresolved) stellar and diffuse ISM background. Nevertheless, employing complete spectroscopic information allows for the investigation of a significant number of PNe in these regions, despite the limited spatial coverage.

Bibliography

G. S. Anand et al. Distances to PHANGS galaxies: New tip of the red giant branch measurements and adopted distances. *Monthly Notices of the Royal Astronomical Society*, 501(3):3621–3639, 11 2020. ISSN 0035-8711. doi: 10.1093/mnras/staa3668. URL https://doi.org/10.1093/mnras/staa3668.

G. Aniano et al. Modeling dust and starlight in galaxies observed by spitzer and herschel: The kingfish sample. *The Astrophysical Journal*, 889(2):150, feb 2020. doi: 10.3847/1538-4357/ab5fdb. URL https://dx.doi.org/10.3847/1538-4357/ab5fdb.

S. Arribas et al. INTEGRAL: an Optical-Fiber System for 2-D Spectroscopy on the 4.2-in William Herschel Telescope. In S. Arribas, E. Mediavilla, and F. Watson, editors, *Fiber Optics in Astronomy III*, volume 152 of *Astronomical Society of the Pacific Conference Series*, page 149, Jan. 1998.

M. Asplund et al. The chemical composition of the sun. *Annual Review of Astronomy and Astrophysics*, 47(1):481–522, 2009. doi: 10.1146/annurev.astro.46.060407.145222. URL https://doi.org/10.1146/annurev.astro.46.060407.145222.

R. Bacon et al. The MUSE second-generation VLT instrument. In I. S. McLean, S. K. Ramsay, and H. Takami, editors, *Ground-based and Airborne Instrumentation for Astronomy III*, volume 7735, page 773508. International Society for Optics and Photonics, SPIE, 2010. doi: 10.1117/12.856027. URL https://doi.org/10.1117/12.856027.

R. Bacon et al. MUSE Commissioning. *The Messenger*, 157:13–16, Sept. 2014.

J. A. Baldwin, M. M. Phillips, and R. Terlevich. Classification parameters for the emission-line spectra of extragalactic objects. *Publications of the Astronomical Society of the Pacific*, 93(551):5, feb 1981. doi: 10.1086/130766. URL https://dx.doi.org/10.1086/130766.

C. M. Baugh et al. Modelling emission lines in star-forming galaxies. *Monthly Notices of the Royal Astronomical Society*, 510(2):1880–1893, 12 2021. ISSN 0035-8711. doi: 10.1093/mnras/stab3506. URL https://doi.org/10.1093/mnras/stab3506.

D. A. Berg et al. Chaos i. direct chemical abundances for regions in ngc 628. *The Astrophysical Journal*, 806(1):16, jun 2015. doi: 10.1088/0004-637X/806/1/16. URL https://dx.doi.org/10.1088/0004-637X/806/1/16.

W. P. Blair and K. S. Long. An optical survey of supernova remnants in m83*. *The Astrophysical Journal Supplement Series*, 155(1):101, nov 2004. doi: 10.1086/423958. URL https://dx.doi.org/10.1086/423958.

G. A. Blanc et al. The VIRUS-P Exploration of Nearby Galaxies (VENGA): Survey Design, Data Processing, and Spectral Analysis Methods. *aj*, 145(5):138, May 2013. doi: 10.1088/0004-6256/145/5/138.

V. V. Bobylev and A. T. Bajkova. Vertical distribution and kinematics of planetary nebulae in the milky way. *Astronomy Letters*, 43(5):304–315, May 2017. doi: 10.1134/s1063773717040028. URL https://doi.org/10.1134/s1063773717040028.

L. Bottinelli et al. HI line studies of galaxies. III. Distance moduli of 822 disk galaxies. *aaps*, 56: 381–413, June 1984.

L. Bottinelli et al. The extragalactic distance scale derived from "sosie" galaxies. I. Distances of

167 galaxies which are sosies of 14 nearby galaxies. *apjs*, 59:293–310, Nov. 1985. doi: 10.1086/191073.

L. Bradley et al. astropy/photutils: v0.6, Jan. 2019. URL https://doi.org/10.5281/zenodo.2533376.

A. Buzzoni, M. Arnaboldi, and R. L. M. Corradi. Planetary nebulae as tracers of galaxy stellar populations. *Monthly Notices of the Royal Astronomical Society*, 368(2):877–894, 04 2006. ISSN 0035-8711. doi: 10.1111/j.1365-2966.2006.10163.x. URL https://doi.org/10.1111/j.1365-2966.2006.10163.x.

Casasola et al. Spectroscopic characterization of the protocluster of galaxies around 7c 1756+6520 at z 1.4. *A&A*, 618:A128, 2018. doi: 10.1051/0004-6361/201833052. URL https://doi.org/10.1051/0004-6361/201833052.

R. Ciardullo. The planetary nebula luminosity function: Pieces of the puzzle. *Publications of the Astronomical Society of Australia*, 27(2):149–155, 2010. doi: 10.1071/AS09022.

R. Ciardullo. The planetary nebula luminosity function at the dawn of gaia. *Astrophysics and Space Science*, 341(1):151–161, Apr. 2012. doi: 10.1007/s10509-012-1061-2. URL https://doi.org/10.1007/s10509-012-1061-2.

R. Ciardullo. The planetary nebula luminosity function. In R. de Grijs, editor, *Advancing the Physics of Cosmic Distances*, volume 289, pages 247–254, Feb. 2013. doi: 10.1017/S1743921312021503.

R. Ciardullo. The planetary nebula luminosity function in the era of precision cosmology. *Frontiers in Astronomy and Space Sciences*, 9, 2022. ISSN 2296-987X. doi: 10.3389/fspas.2022.896326. URL https://www.frontiersin.org/articles/10.3389/fspas.2022.896326.

R. Ciardullo et al. Planetary Nebulae as Standard Candles. II. The Calibration in M31 and Its Companions. *apj*, 339:53, Apr. 1989. doi: 10.1086/167275.

R. Ciardullo, G. H. Jacoby, and J. L. Tonry. A Comparison of the Planetary Nebula Luminosity Function and Surface Brightness Fluctuation Distance Scales. *apj*, 419:479, Dec. 1993. doi: 10.1086/173501.

R. Ciardullo et al. Planetary nebulae as standard candles. xii. connecting the population i and population ii distance scales. *The Astrophysical Journal*, 577(1):31, sep 2002. doi: 10.1086/342180. URL https://dx.doi.org/10.1086/342180.

R. Ciardullo et al. Close binaries as the progenitors of the brightest planetary nebulae. *The Astrophysical Journal*, 629(1):499, aug 2005. doi: 10.1086/431353. URL https://dx.doi.org/10.1086/431353.

B. D. Davis et al. The planetary nebula luminosity function (pnlf): Contamination from supernova remnants. *Research Notes of the AAS*, 2(1):32, feb 2018. doi: 10.3847/2515-5172/aab045. URL https://dx.doi.org/10.3847/2515-5172/aab045.

Dessart and Hillier. Distance determinations using type ii supernovae and the expanding photosphere method. *A&A*, 439(2):671–685, 2005. doi: 10.1051/0004-6361:20053217. URL https://doi.org/10.1051/0004-6361:20053217.

M. A. Dopita, G. H. Jacoby, and E. Vassiliadis. A Theoretical Calibration of the Planetary Nebular Cosmic Distance Scale. *apj*, 389:27, Apr. 1992. doi: 10.1086/171186.

J. J. D'Agostino et al. Comparison of theoretical starburst photoionization models for optical diagnostics. *The Astrophysical Journal*, 878(1):2, jun 2019. doi: 10.3847/1538-4357/ab1d5e. URL https://dx.doi.org/10.3847/1538-4357/ab1d5e.

Emsellem et al. The phangs-muse survey - probing the chemo-dynamical evolution of disc galaxies. *A&A*, 659:A191, 2022. doi: 10.1051/0004-6361/202141727. URL https://doi.org/10.1051/0004-6361/202141727.

J. J. Feldmeier, R. Ciardullo, and G. H. Jacoby. The planetary nebula distance to m101. *The Astrophysical Journal*, 461(1):L25, apr 1996. doi: 10.1086/309994. URL https://dx.doi.org/10.1086/

309994.

J. J. Feldmeier, R. Ciardullo, and G. H. Jacoby. Planetary nebulae as standard candles. xi. application to spiral galaxies. *The Astrophysical Journal*, 479(1):231, apr 1997. doi: 10.1086/512787. URL https://dx.doi.org/10.1086/512787.

J. J. Feldmeier, G. H. Jacoby, and M. M. Phillips. Calibrating type ia supernovae using the planetary nebula luminosity function. i. initial results*. *The Astrophysical Journal*, 657(1):76, mar 2007a. doi: 10.1086/510897. URL https://dx.doi.org/10.1086/510897.

J. J. Feldmeier, G. H. Jacoby, and M. M. Phillips. Calibrating type ia supernovae using the planetary nebula luminosity function. i. initial results*. *The Astrophysical Journal*, 657(1):76, mar 2007b. doi: 10.1086/510897. URL https://dx.doi.org/10.1086/510897.

L. Ferrarese et al. A database of cepheid distance moduli and tip of the red giant branch, globular cluster luminosity function, planetary nebula luminosity function, and surface brightness fluctuation data useful for distance determinations. *The Astrophysical Journal Supplement Series*, 128(2): 431, jun 2000. doi: 10.1086/313391. URL https://dx.doi.org/10.1086/313391.

N. A. Franchetti et al. Physical structure and nature of supernova remnants in m101. *The Astronomical Journal*, 143(4):85, mar 2012. doi: 10.1088/0004-6256/143/4/85. URL https://dx.doi.org/10.1088/0004-6256/143/4/85.

W. L. Freedman. Measurements of the hubble constant: Tensions in perspective. *The Astrophysical Journal*, 919(1):16, Sept. 2021. doi: 10.3847/1538-4357/ac0e95. URL https://doi.org/10.3847/1538-4357/ac0e95.

W. L. Freedman and B. F. Madore. The hubble constant. *Annual Review of Astronomy and Astrophysics*, 48(1):673–710, 2010. doi: 10.1146/annurev-astro-082708-101829. URL https://doi.org/10.1146/annurev-astro-082708-101829.

D. J. Frew and Q. A. Parker. Planetary nebulae: Observational properties, mimics and diagnostics. *Publications of the Astronomical Society of Australia*, 27(2):129–148, 2010. doi: 10.1071/AS09040.

R. Giovanelli et al. Extinction in SC Galaxies. *aj*, 107:2036, June 1994. doi: 10.1086/117014.

R. Giovanelli et al. The motions of clusters of galaxies and the dipoles of the peculiar velocity field. *The Astronomical Journal*, 116(6):2632–2643, Dec. 1998. doi: 10.1086/300652. URL https://doi.org/10.1086/300652.

Hartke et al. The halo of mand its environment as traced by planetary nebulae populations. *A&A*, 603: A104, 2017. doi: 10.1051/0004-6361/201730463. URL https://doi.org/10.1051/0004-6361/201730463.

M. A. Hendry et al. A study of the Type II-P supernova 2003gd in M74. *Monthly Notices of the Royal Astronomical Society*, 359(3):906–926, 05 2005. ISSN 0035-8711. doi: 10.1111/j.1365-2966.2005.08928.x. URL https://doi.org/10.1111/j.1365-2966.2005.08928.x.

K. A. Herrmann and R. Ciardullo. Planetary nebulae in face-on spiral galaxies. iii. planetary nebula kinematics and disk mass. *The Astrophysical Journal*, 705(2):1686, oct 2009. doi: 10.1088/0004-637X/705/2/1686. URL https://dx.doi.org/10.1088/0004-637X/705/2/1686.

K. A. Herrmann et al. Planetary Nebulae in Face-On Spiral Galaxies. I. Planetary Nebula Photometry and Distances. *apj*, 683(2):630–643, Aug. 2008. doi: 10.1086/589920.

L. C. Ho, A. V. Filippenko, and W. L. W. Sargent. A Search for "Dwarf" Seyfert Nuclei. III. Spectroscopic Parameters and Properties of the Host Galaxies. *apjs*, 112(2):315–390, Oct. 1997. doi: 10.1086/313041.

S. B. Howell. Two-dimensional aperture photometry: Signal-to-noise ratio of point-source observations and optimal data-extraction techniques. *Publications of the Astronomical Society of the Pacific*, 101(640):616, jun 1989. doi: 10.1086/132477. URL https://dx.doi.org/10.1086/132477.

I. Iben and A. Renzini. Asymptotic giant branch evolution and beyond. *Annual Review of Astronomy and Astrophysics*, 21(1):271–342, 1983. doi: 10.1146/annurev.aa.21.090183.001415. URL https://doi.org/10.1146/annurev.aa.21.090183.001415.

B. A. Jacobs et al. The extragalactic distance database: Color–magnitude diagrams. *The Astronomical Journal*, 138(2):332, jun 2009. doi: 10.1088/0004-6256/138/2/332. URL https://dx.doi.org/10.1088/0004-6256/138/2/332.

G. H. Jacoby. Planetary Nebulae as Standard Candles. I. Evolutionary Models. *apj*, 339:39, Apr. 1989. doi: 10.1086/167274.

G. H. Jacoby and O. D. Marco. A survey for very faint planetary nebulae in the smc. i. identification, confirmation, and preliminary analysis*. *The Astronomical Journal*, 123(1):269, jan 2002. doi: 10.1086/324737. URL https://dx.doi.org/10.1086/324737.

G. H. Jacoby et al. A critical review of selected techniques for measuring extragalactic distances. *Publications of the Astronomical Society of the Pacific*, 104(678):599, aug 1992. doi: 10.1086/133035. URL https://dx.doi.org/10.1086/133035.

I. S. Jang and M. G. Lee. The tip of the red giant branch distance to the perfect spiral galaxy m74 hosting three core-collapse supernovae. *The Astrophysical Journal*, 792(1):52, aug 2014. doi: 10.1088/0004-637X/792/1/52. URL https://dx.doi.org/10.1088/0004-637X/792/1/52.

Jenner. The Expanding Shell of Nova DQ Herculis 1934. In *Bulletin of the American Astronomical Society*, volume 10, page 427, Mar. 1978.

D. Kasen and S. E. Woosley. Type II Supernovae: Model Light Curves and Standard Candle Relationships. *apj*, 703(2):2205–2216, Oct. 2009. doi: 10.1088/0004-637X/703/2/2205.

G. Kauffmann et al. The host galaxies of active galactic nuclei. *Monthly Notices of the Royal Astronomical Society*, 346(4):1055–1077, 12 2003. ISSN 0035-8711. doi: 10.1111/j.1365-2966.2003.07154.x. URL https://doi.org/10.1111/j.1365-2966.2003.07154.x.

L. J. Kewley et al. Theoretical modeling of starburst galaxies. *The Astrophysical Journal*, 556(1):121, jul 2001. doi: 10.1086/321545. URL https://dx.doi.org/10.1086/321545.

L. J. Kewley et al. The host galaxies and classification of active galactic nuclei. *mnras*, 372(3):961–976, Nov. 2006. doi: 10.1111/j.1365-2966.2006.10859.x.

K. Kreckel et al. Characterizing spiral arm and interarm star formation. *The Astrophysical Journal*, 827(2):103, aug 2016. doi: 10.3847/0004-637X/827/2/103. URL https://dx.doi.org/10.3847/0004-637X/827/2/103.

K. Kreckel et al. A REVISED PLANETARY NEBULA LUMINOSITY FUNCTION DISTANCE TO NGC 628 USING MUSE. *The Astrophysical Journal*, 834(2):174, Jan. 2017. doi: 10.3847/1538-4357/834/2/174. URL https://doi.org/10.3847/1538-4357/834/2/174.

K. Kreckel et al. Mapping metallicity variations across nearby galaxy disks. *The Astrophysical Journal*, 887(1):80, dec 2019. doi: 10.3847/1538-4357/ab5115. URL https://dx.doi.org/10.3847/1538-4357/ab5115.

P. Lang et al. Phangs co kinematics: Disk orientations and rotation curves at 150 pc resolution. *The Astrophysical Journal*, 897(2):122, jul 2020. doi: 10.3847/1538-4357/ab9953. URL https://dx.doi.org/10.3847/1538-4357/ab9953.

L. Li et al. Three-dimensional structure of the milky way dust: Modeling of lamost data. *The Astrophysical Journal*, 858(2):75, may 2018. doi: 10.3847/1538-4357/aabaef. URL https://dx.doi.org/10.3847/1538-4357/aabaef.

N. Li et al. Estimating Dust Attenuation from Galactic Spectra. I. Methodology and Tests. *apj*, 896(1):38, June 2020. doi: 10.3847/1538-4357/ab92a1.

N. Li et al. Estimating Dust Attenuation From Galactic Spectra. II. Stellar and Gas Attenuation in Star-forming and Diffuse Ionized Gas Regions in MaNGA. *apj*, 917(2):72, Aug. 2021. doi:

10.3847/1538-4357/ac0973.

N. Y. Lu et al. H i 21 Centimeter Observations and I-Band CCD Surface Photometry of Spiral Galaxies behind the Virgo Cluster and toward Its Antipode. *apjs*, 88:383, Oct. 1993. doi: 10.1086/191826.

Marigo et al. Evolution of planetary nebulae - ii. population effects on the bright cut-off of the pnlf. *A&A*, 423(3):995–1015, 2004. doi: 10.1051/0004-6361:20040234. URL https://doi.org/10.1051/0004-6361:20040234.

K. B. W. McQuinn et al. Accurate Distances to Important Spiral Galaxies: M63, M74, NGC 1291, NGC 4559, NGC 4625, and NGC 5398. *aj*, 154(2):51, Aug. 2017a. doi: 10.3847/1538-3881/aa7aad.

K. B. W. McQuinn et al. Accurate Distances to Important Spiral Galaxies: M63, M74, NGC 1291, NGC 4559, NGC 4625, and NGC 5398. *aj*, 154(2):51, Aug. 2017b. doi: 10.3847/1538-3881/aa7aad.

K. B. W. McQuinn et al. Accurate distances to important spiral galaxies: M63, m74, ngc 1291, ngc 4559, ngc 4625, and ngc 5398*. *The Astronomical Journal*, 154(2):51, jul 2017. doi: 10.3847/1538-3881/aa7aad. URL https://dx.doi.org/10.3847/1538-3881/aa7aad.

R. H. Méndez. The Planetary Nebulae Luminosity Function (PNLF): current perspectives. In X. Liu, L. Stanghellini, and A. Karakas, editors, *Planetary Nebulae: Multi-Wavelength Probes of Stellar and Galactic Evolution*, volume 323, pages 298–302, Oct. 2017. doi: 10.1017/S1743921317000461.

J. C. Muñoz-Mateos et al. Radial Distribution of Stars, Gas, and Dust in Sings Galaxies. II. Derived Dust Properties. *apj*, 701(2):1965–1991, Aug. 2009. doi: 10.1088/0004-637X/701/2/1965.

R. H. Méndez et al. Detection, photometry, and slitless radial velocities of 535 planetary nebulae in the flattened elliptical galaxy ngc 4697*. *The Astrophysical Journal*, 563(1):135, dec 2001. doi: 10.1086/323794. URL https://dx.doi.org/10.1086/323794.

Olivares et al. The standardized candle method for type ii plateau supernovae. *The Astrophysical Journal*, 715(2):833, may 2010. doi: 10.1088/0004-637X/715/2/833. URL https://dx.doi.org/10.1088/0004-637X/715/2/833.

B. Paczyński. Evolution of Single Stars. VI. Model Nuclei of Planetary Nebulae. *actaa*, 21:417, Jan. 1971.

H. Riesgo and J. A. López. Revised Diagnostic Diagrams for Planetary Nebulae. *rmxaa*, 42:47–51, Apr. 2006. doi: 10.48550/arXiv.astro-ph/0602201.

Ó. Rodríguez, A. Clocchiatti, and M. Hamuy. Photospheric Magnitude Diagrams for Type II Supernovae: A Promising Tool to Compute Distances. *aj*, 148(6):107, Dec. 2014. doi: 10.1088/0004-6256/148/6/107.

M. Romaniello et al. Enhanced Data Discovery Services for the ESO Science Archive. *The Messenger*, 172:2–7, June 2018. doi: 10.18727/0722-6691/5073.

Roth et al. Muse crowded field 3d spectroscopy in ngc 300 - i. first results from central fields. *A&A*, 618:A3, 2018. doi: 10.1051/0004-6361/201833007. URL https://doi.org/10.1051/0004-6361/201833007.

M. M. Roth et al. Spectrophotometry of planetary nebulae in the bulge of m31. *The Astrophysical Journal*, 603(2):531, mar 2004. doi: 10.1086/381526. URL https://dx.doi.org/10.1086/381526.

M. M. Roth et al. Pmas: The potsdam multi-aperture spectrophotometer. i. design, manufacture, and performance. *Publications of the Astronomical Society of the Pacific*, 117(832):620, may 2005. doi: 10.1086/429877. URL https://dx.doi.org/10.1086/429877.

M. M. Roth et al. Toward precision cosmology with improved PNLF distances using VLT-MUSEI. methodology and tests. *The Astrophysical Journal*, 916(1):21, July 2021. doi: 10.3847/1538-4357/ac02ca. URL https://doi.org/10.3847/1538-4357/ac02ca.

F. Sabbadin, S. Minello, and A. Bianchini. Sharpless 176: a large, nearby planetary nebula. *aap*, 60: 147–149, Aug. 1977.

E. Sabbi et al. The resolved stellar populations in the legus galaxies1*. *The Astrophysical Journal Supplement Series*, 235(1):23, mar 2018a. doi: 10.3847/1538-4365/aaa8e5. URL https://dx.doi.org/10.3847/1538-4365/aaa8e5.

E. Sabbi et al. The resolved stellar populations in the legus galaxies1*. *The Astrophysical Journal Supplement Series*, 235(1):23, mar 2018b. doi: 10.3847/1538-4365/aaa8e5. URL https://dx.doi.org/10.3847/1538-4365/aaa8e5.

L. Sabin et al. New Galactic supernova remnants discovered with IPHAS. *Monthly Notices of the Royal Astronomical Society*, 431(1):279–291, 02 2013. ISSN 0035-8711. doi: 10.1093/mnras/stt160. URL https://doi.org/10.1093/mnras/stt160.

A. Sandage and G. A. Tammann. Steps toward the Hubble constant. IV. Distances to 39 galaxies in the general field leading to a calibration of the galaxy luminosity classes and a first hint of the value of H_0. *apj*, 194:559–568, Dec. 1974. doi: 10.1086/153275.

Santoro, Francesco et al. Phangs-muse: The hregion luminosity function of local star-forming galaxies. *A&A*, 658:A188, 2022. doi: 10.1051/0004-6361/202141907. URL https://doi.org/10.1051/0004-6361/202141907.

M. Sarzi et al. The planetary nebulae population in the central regions of M32: the SAURON view. *Monthly Notices of the Royal Astronomical Society*, 415(3):2832–2843, 08 2011. ISSN 0035-8711. doi: 10.1111/j.1365-2966.2011.18900.x. URL https://doi.org/10.1111/j.1365-2966.2011.18900.x.

F. Scheuermann et al. Planetary nebula luminosity function distances for 19 galaxies observed by PHANGS–MUSE. *Monthly Notices of the Royal Astronomical Society*, 511(4):6087–6109, Jan. 2022. doi: 10.1093/mnras/stac110. URL https://doi.org/10.1093/mnras/stac110.

E. F. Schlafly and D. P. Finkbeiner. Measuring reddening with sloan digital sky survey stellar spectra and recalibrating sfd. *The Astrophysical Journal*, 737(2):103, aug 2011. doi: 10.1088/0004-637X/737/2/103. URL https://dx.doi.org/10.1088/0004-637X/737/2/103.

Schönberner et al. The evolution of planetary nebulae* - iv. on the physics of the luminosity function. *A&A*, 473(2):467–484, 2007. doi: 10.1051/0004-6361:20077437. URL https://doi.org/10.1051/0004-6361:20077437.

Schönberner et al. The evolution of planetary nebulae - vii. modelling planetary nebulae of distant stellar systems. *A&A*, 523:A86, 2010. doi: 10.1051/0004-6361/200913427. URL https://doi.org/10.1051/0004-6361/200913427.

M. E. Sharina, I. D. Karachentsev, and N. A. Tikhonov. Photometric distances to NGC 628 and its four companions. *aaps*, 119:499–507, Nov. 1996.

P. A. Shaver et al. The galactic abundance gradient. *Monthly Notices of the Royal Astronomical Society*, 204(1):53–112, 09 1983. ISSN 0035-8711. doi: 10.1093/mnras/204.1.53. URL https://doi.org/10.1093/mnras/204.1.53.

E. J. Shaya et al. Action dynamics of the local supercluster. *The Astrophysical Journal*, 850(2): 207, dec 2017. doi: 10.3847/1538-4357/aa9525. URL https://dx.doi.org/10.3847/1538-4357/aa9525.

O. K. Sil'chenko and V. L. Afanasiev. Decoupled nuclei and nuclear polar rings in regular spiral galaxies NGC 7217. *aap*, 364:479–490, Dec. 2000.

A. A. Soemitro et al. VizieR Online Data Catalog: MUSE-PN Catalogue of NGC 300 (Soemitro+, 2023). *VizieR Online Data Catalog*, art. J/A+A/671/A142, Jan. 2023.

Y.-J. Sohn and T. Davidge. Multicolor ccd photometry of supergiants in the disk of ngc 628. *aj*, 111: 2280, June 1996. doi: 10.1086/117962.

Spriggs et al. Fornax 3d project: Automated detection of planetary nebulae in the centres of early-type galaxies and first results. *A&A*, 637:A62, 2020. doi: 10.1051/0004-6361/201936862. URL https://doi.org/10.1051/0004-6361/201936862.

P. B. Stetson. DAOPHOT - a computer program for crowded-field stellar photometry. *Publications of the Astronomical Society of the Pacific*, 99:191, Mar. 1987. doi: 10.1086/131977. URL https://doi.org/10.1086/131977.

A. M. Teodorescu et al. Planetary nebulae in the elliptical galaxy ngc 4649 (m 60): Kinematics and distance redetermination*. *The Astrophysical Journal*, 736(1):65, jul 2011. doi: 10.1088/0004-637X/736/1/65. URL https://dx.doi.org/10.1088/0004-637X/736/1/65.

J. L. Tonry et al. The surface brightness fluctuation survey of galaxy distances. II. local and large-scale flows. *The Astrophysical Journal*, 530(2):625–651, Feb. 2000. doi: 10.1086/308409. URL https://doi.org/10.1086/308409.

R. B. Tully. *Nearby galaxies catalog*. 1988.

S. D. Van Dyk, W. Li, and A. V. Filippenko. The light echo around supernova 2003gd in messier 74. *pasp*, 118(841):351–357, Mar. 2006. doi: 10.1086/500225.

E. Vassiliadis and P. R. Wood. Post–Asymptotic Giant Branch Evolution of Low- to Intermediate-Mass Stars. *apjs*, 92:125, May 1994. doi: 10.1086/191962.

Ventimiglia, Arnaboldi, and Gerhard. The unmixed kinematics and origins of diffuse stellar light in the core of the hydra i cluster (abell 1060). *A&A*, 528:A24, 2011. doi: 10.1051/0004-6361/201015982. URL https://doi.org/10.1051/0004-6361/201015982.

Vinkó, J. et al. Distance of the hypernova sn 2002ap via the expanding photosphere method*. *A&A*, 427(2):453–464, 2004. doi: 10.1051/0004-6361:20040272. URL https://doi.org/10.1051/0004-6361:20040272.

P. M. Weilbacher et al. The data processing pipeline for the MUSE instrument. *aap*, 641:A28, Sept. 2020. doi: 10.1051/0004-6361/202037855.

H. F. M. Yao et al. Galaxy and mass assembly (gama): A wise study of the activity of emission-line systems in g23. *The Astrophysical Journal*, 903(2):91, nov 2020. doi: 10.3847/1538-4357/abba1a. URL https://dx.doi.org/10.3847/1538-4357/abba1a.

H. J. Zahid et al. Stellar Absorption Line Analysis of Local Star-forming Galaxies: The Relation between Stellar Mass, Metallicity, Dust Attenuation, and Star Formation Rate. *apj*, 847(1):18, Sept. 2017. doi: 10.3847/1538-4357/aa88ae.

A. V. Zasov and D. V. Bizyaev. An estimate for the Hubble constant using a criterion for gravitational stability of gaseous disks. *Astronomy Letters*, 22(1):71–78, Jan. 1996.